INTERNATIONAL ATOMIC ENERGY AGENCY
UNITED NATIONS EDUCATIONAL, SCIENTIFIC AND CULTURAL ORGANIZATION

INTERNATIONAL CENTRE FOR THEORETICAL PHYSICS
34100 TRIESTE (ITALY) - P.O.B. 586 - MIRAMARE - STRADA COSTIERA 11 - TELEPHONE: 2240-1
CABLE: CENTRATOM - TELEX 460392-I

H4.SMR/381-27

COLLEGE ON ATOMIC AND MOLECULAR PHYSICS: PHOTON ASSISTED COLLISIONS IN ATOMS AND MOLECULES

(30 January - 24 February 1989)

HOW TO ATTACK COMPLEX GAS PHASE COMBUSTION SYSTEMS

J. WOLFRUM

Universitat Heidelberg
Physikalisch-Chemisches Institut
Heidelberg D 6900
F.R. Germany

HOW TO ATTACK COMPLEX GAS PHASE COMBUSTION SYSTEMS

Jürgen Wolfrum
Physikalisch-Chemisches Institut
Universität Heidelberg

Summary

Starting from detailed investigations of elementary chemical reactions a strategy for experimental and theoretical analysis of complex combustion systems is described. Experimental results on the effect of selective translational excitation of reactants in the reaction $H + O_2 \rightarrow OH + O$ are compared with theoretical studies on ab initio potential energy surfaces. For the reaction $CN + H_2O \rightarrow HCN + OH$ direct measurements of thermal rates in shock tubes are compared with data obtained from a laser-photolysis laser-induced fluorescence technique .

The attack of practical combustion problems with homogeneous models including detailed chemistry is described for the NO_x-reduction in power plants and the auto-ignition of hydrocarbon-air mixtures in relation to engine knock. Next the interaction of elementary chemical processes with steady and unsteady laminar flows is considered. Laminar counter-flow diffusion flames constitute an important basis set for the simulation of more complicated turbulent combustion processes. Having a library of pre-calculated "flamelets" of different strain rate and fuel/oxidizer mixture compositions the numerical treatment of turbulent flame structures can be done on existing computers. Detailed calculations on pure and partially premixed CH_4/air counter-flow diffusion flames are compared with results of non-intrusive CARS measurements for various strain rates. For the unsteady case as a simple test system the ignition of O_2/O_3 mixtures by irradiation with a CO_2-laser along the axis of a cylindrical vessel is considered. Mathematical simulation of the ignition process is done by solving the corresponding system of conservation equations. Spatial discretization using definite differences leads to a system of ordinary differential and algebraic equations which can be solved numerically. Experimental data are presented for velocity components of the flame front from IR-UV double resonance experiments.

The last part describes two approaches to link complex chemistry to models of turbulent flow field predictions applied to an enclosed turbulent jet diffusion flame. One is a conserved-scalar approach employing a stretched-laminar-flamelet model, the other involves a direct closure of the chemical production terms by a pdf-method. Numerical results for turbulent CO/air diffusion flames and experimental results on imaging of laminar and turbulent flame fronts by OH radical and acetaldehyde fluorescence in an internal combustion engine are presented.

1. Introduction

Experimental possibilities to study complex combustion systems in detail have expanded quite dramatically in recent years as a result of the development of various laser sources with high temporal, spectral and spatial resolution. Beside illuminating microscopic details, laser spectroscopic methods are especially important for non-intrusive measurements in practical systems in which chemical kinetics is coupled with transport processes. Data gained from such experiments are the basis for comparison with detailed mathematical modelling of chemical processes in laminar and turbulent flows including heat and species transport. The present paper can, however, by far not give a comprehensive compilation of experimental and theoretical results in this broad field. Instead, as requested by the organizers of the symposium, a number of typical examples mostly from the laboratory of the author are described.
As illustrated in Fig. 1, the examples are arranged in an increasing order of complexity.

2. Microscopic Dynamic of Elementary Chemical Reactions

Despite the large number of elementary reactions taking place in the oxidation of hydrocarbons, important parameters of the combustion process are controlled by few elementary reactions. Sensitivity analysis shows that calculated flame velocities are relatively independent from reactions specifically for the oxidation of the fuel molecules. However, there is a strong influence on the calculated flame velocity from unspecific reactions such as the reaction of hydrogen atoms with oxygen molecules /1,2/.

$$H + O_2 \rightarrow OH + O \qquad \Delta H^\circ_8 = -69{,}5\ kJ\ mol^{-1} \qquad (1)$$

This endothermic reaction leads to the formation of two radicals and is therefore a very important chain-branching step. As shown in Fig. 2, the dynamics of such an elementary reaction with a high energy barrier can be studied in microscopic detail by combining translationally hot atom formation from laser photolysis with time-, state- and orientation-resolved product detection by laser induced fluorescence spectroscopy.
The apparatus is depicted in Fig. 3. Two laser beams are directed perpendicular through a flow reactor equipped with long side arms to reduce the scattered light from the dye laser analysis pulse. The dye laser operates with

Rodamine 640 and a frequency doubling KDP crystal to generate a pulse in the 306-311 nm region to probe OH radicals by laser induced fluorescence. Fluorescence light is then detected as a function of the dye laser wavelength through emission optics and a filter transmitting between 240 and 390 nm and by a photomultiplier.

Fig. 4a gives examples of the OH nascent rotational state distributions at different collision energies /3/. The major part of the relative translational energy of the reactants is converted into rotational energy of the product OH in agreement with the results of quasi-classical trajectory calculations /4/. The observed rotational energy distributions give interesting microscopic details on the molecular dynamics of these elementary steps. Spin-orbit and orbital-rotation interactions in the OH radical cause fine structure splittings for each rotational level. Each of these fine structure levels can be probed by different rotational subbands. The two OH spin states $^2\Pi_{1/2}$ and $^2\Pi_{3/2}$ are, within experimental error, equally populated. However, as shown in Fig. 4b, the Λ-doublet fine structure states show a clear preference for the lower energy Π^+ (A') component. The experimental results indicate that break-up of the reaction complex generates forces in a plane containing the bond to be broken. The OH radical rotates in that plane and J_{OH} is perpendicular to it and to the broken bond. This picture is consistent with a preferential planar exit channel in these reactions. This could also be directly demonstrated by using polarized photolysis and analysis laser beams /5/. The physical difference between the two Λ-doublet components Π^+ (A') and Π^- (A'') arises from interaction of the electronic spin-orbit momentum with the rotation of the molecule. For fast rotation of the OH radical, the unpaired electron in the p orbital of the oxygen is no longer able to follow the movement of the atomic nuclei. If the p orbital lies in the OH rotational plane, the electron distribution on the oxygen atom changes, becoming increasingly spherical. In contrast, for a Π^- (A'') configuration, the oxygen atom moves in the nodal plane of the p orbital and thus continues to "see" a dumbbell-shaped electron environment, even for fast rotation. This leads to a splitting of the energies of the Π^+ (A') and Π^- (A'') configurations, which selectively increases with increasing rotational energy. As shown in Fig. 4b at 1,8 eV collision energy, about three OH radicals were found in the Π^+ (A') state for each OH radical in the Π^- (A'') state. This shows that the unpaired electron formed after bond cleavage of O_2 stays in an orbital in the rotational plane of the OH radical. During the reaction, most of the HO_2 complexes do not rotate

out of the initial plane, which car be understood on kinematic grounds /6/. Reaction (1) is known to take place adiabatically on the ground-state potential surface of the HO_2 ($^2A''$) radical. Experimentally a total reaction cross-section of 0.42 +0.2 $Å^2$ at E = 2.6 eV is found /3/. The theoretical reactive cross-section obtained under these conditions by quasi-classical trajectory calculations /4,7/ on the Melius-Blint /8/ surface is 0.38 $Å^2$. These numbers cannot be compared directly, because the multiplicity of the $^2A''$ surface of HO_2 is not taken into account /2,. The observed discrepancies may be attributed to a reduction of calculated reaction cross-section due to a "rigid" character and a barrier of 8 kJ mol^{-1} in the Melius-Blint surface for dissociation of the HO_2 in the reaction $HO_2 + M \rightarrow H + O_2 + M$ /9/. Later calculations /10,11/ reduce this barrier. Also for the reaction (-1) $O + OH \rightarrow O_2 + H$ the Melius-Blint surface apparantly overestimates the long-range O-OH attraction, while the Quack-Troe interpolation scheme leads to better agreement with the expe-imental values at low temperature if the two lowest electronic states of the HO_2 radical are taken into account /9/. Calculated rate coefficients obtained by using this theoretical cross sections from the surface /8/ are in agreement with shock tube measurements for k_1 by Schott /12/. However, as shown in Fig. 5, recent shock tube experiments /13,14/ using time-resolved atomic resonance line absorption give higher values for k_1 in agreement with the reactive cross sections obtained in state selected experiments /3/. This example shows that even for a very simple but extremely important chemical elementary step in combustion more work has to be done on the potential energy surface to obtain a satisfactory agreement between the results from quantum chemistry and state selective and thermal experiments.

3. Direct Measurement of Thermal Rate Constants

The main basis for detailed chemical kinetic modelling of combustion processes are still careful direct measurements of thermal rate constants over a wide temperature and pressure range. As an example of an important area of chemical modelling some elementary reactions taking place in the conversion of fuel nitrogen to nitric oxide are shown in Fig. 6. One interesting step is the reaction

$$OH + HCN \rightarrow H_2C + CN \qquad (2)$$

Direct experimental investigations on the Arrhenius parameters for this reaction are hampered by the fact that at low temperatures the addition of the OH radical dominates over the abstraction reaction. It is therefore difficult to extrapolate rate data to higher temperatures. A more direct access to the reaction are investigations of the reverse step which has been carried out at higher temperatures in shock tube experiments /17/. This studies cover however only a small part in the 1/T Arrhenius plot which makes it difficult to extrapolate with sufficient accuracy to lower temperatures. New ways for direct measurements of such reactions are offered by employing a laser photolysis-laser induced fluorescence (LIF) technique (s. Fig. 7).

An ArF excimer laser (Lambda EMG 501) delivered the photolysis beam at 193 nm. A circular diaphragm shaped a homogeneously irradiated beam of 4 mm diameter with typically 2-3 mJ energy. A frequency-doubled pulsed dye laser (Lambda FL 2002 EC) pumped by a XeCl excimer laser and working with sulforhodamin B emitted light in the region 305-320 nm, which was used to excite the OH-radicals. A second dye laser (Lambda FL 2002, tuning range: 370-400 nm) excited the CN-radicals. To work in the linear region both probe lasers were attenuated and expanded. The emitted fluorescence was collected by a lens (f=D=50 mm) perpendicular to the axis of the laser beams. The apparatus is controlled by a microcomputer (HP9816) via a data acquisition and control unit (HP 3497A). The two laser systems and the boxcar were triggered by a software initiated pulse, distributed by a delay generator. The probe energy and the fluorescence signal were detected by a two channel boxcar and stored by the HP 3497A. The quartz reactor was fitted in a 60 cm long silver tube to insure a homogenous temperature profile. The whole system was heated by means of an accurately thermostated furnace. The temperature gradient along the quartz tube was determined to be less than 1% at temperatures up to 1100 K. Experiments were carried out under conditions, such that each photolysis pulse initiated the reaction within a locally fresh gas mixture. This procedure eliminates kinetic complications caused by unwanted accumulation of photolysis or reaction products.

Shock tube measurements /17/ indicate that the rate constant k_{-2} is approximately two orders of magnitude slower between 500 and 1000 K compared with the rapid radical-radical reaction OH + CN $\rightarrow$ OCN + H. In order to suppress the influence of this competing reaction high H_2O partial pressures must be used in low temperature experiments. Because of the strong fluorescence

quenching behaviour of water the CN and OH LIF detection sensitivity is diminished by at least two orders of magnitude. Due to the low absorption coefficient of C_2N_2 at 193 nm cyanogen pressures around 0.3 Torr are needed to obtain sufficient fluorescence intensities. Rate constants extracted from the (CN (v=0))-decay plots coincide within the error limits with the (OH)-rise measurements. An initial non-thermal vibrational distribution of the CN radicals does not interfere the determination of the rate constant via OH detection. Adding certain amounts of NO as an efficient CN (v=1) quencher vibrational relaxation is complete within the few µs. The observed OH-rise rates were identical to those observed in experiments done without NO. Fig. 8a shows the experimental data between 295 and 1030 K. The Arrhenius plot is linear in this temperature range and yields the rate coefficient expression:

$$k_{-2} = (8.0 \pm 0.8) \times 10^{12} \exp(-(31.2 \pm 0.6)\ \mathrm{kJ/RT})\ \mathrm{cm^3\ mol^{-1}s^{-1}}$$

The shock tube results are also included. These data points fit well to the Arrhenius expression, although Szekely et al. /17/ obtained different Arrhenius parameters ($k_{-2} = 2.3 \times 10^{13} \exp(-55.7\ \mathrm{kJ/RT})\ \mathrm{cm^3 mol^{-1}s^{-1}}$). From thermodynamical properties one can calculate the Arrhenius expression for the reverse reaction (2):

$$k_2 = (7.7 \pm 1) \times 10^{12} \exp(-34.6 \pm 1)\ \mathrm{kJ/RT})\ \mathrm{cm^3\ mol^{-1}s^{-1}}$$

The error limits reflect the uncertainty in both, k_2 and the equilibrium constant K_2. In particular, the heat of formation of CN is subject to some uncertainty. The result agrees with the suggestions of Fritz et al. /15/ and points out the preference of the abstraction channel as the main high temperature pathway. A recent theoretical study /19/ predicts much to low rate constants in this temperature range (see Fig. 8b).

4. Application of homogeneous modeling to practical combustion systems

The simplest form of modeling combustion chemistry is the application of kinetic models under conditions were interactions between various transport processes and elementary chemical reactions have not to be considered. Under certain circumstances such situations with nearly homogeneous temperature and density distributions can be found even in practical combustion systems. Two examples are discussed here.

A. Selective reduction of NO_x in power plants

Inhibition and sensitization of chemical processes by nitric oxide are well-known phenomena. Recently the role of the nitrogen oxides in the formation of acid rain, photochemical smog and the possible depletion of the stratospheric ozone layer has stimulated the interest in chemical reactions which can selectively remove nitrogen oxides. An interesting elementary chemical reaction in this respect is the reaction of nitric oxide with the NH_2 radical. First direct studies of the rate and products of this reaction showed a very fast complex-addition-rearrangement sequence which forms nitrogen molecules and highly vibrational excited water molecules in the single step /20/

$$NH_2 + NO \rightarrow N_2 + H_2O^* \qquad (3)$$

Later investigations with various experimental methods showed different amounts of OH radicals formed in this reaction /21-26/. Recent studies /24-26/ restrict this channel to about 10% at room temperature with no drastic increase up to 1100K /26/. Modeling the NH_3-NO-O_2 reaction system at 1000-1500 K /27,28/ requires higher branching ratios in this temperature range to explain the selective reduction of NO by NH_3 /29/. Theoretical calculations of the potential energy barriers for the various channels are in agreement with the two possibilities /30/. However, since this branching ratio is determined by small energy differences no quantitative answer can be obtained in this way. Using time-resolved infrared emission combined with laser photolysis direct measurements of the distribution of reaction energy in the water molecule formed in reaction (3) can be carried out /31/. An enlarged volume for the production of NH_2 radicals by photolysis of NH_3 is created by multireflection of an ArF-Exciplexlaser beam combined with a Welsh-mirror light gathering system for the effective collection of infrared fluorescence from excited H_2O molecules. The spectrally resolved infrared emission can approximately be simulated with a vibrational temperature for the H_2O molecules formed of 10^4 K. Significantly lower vibrational temperatures are found in the nitrogen molecules by CARS spectroscopy The reaction (3) is very selective in channeling the available reaction energy preferably in the stretching vibrations of one reaction product. Therefore, as shown in Fig. 9 many simultaneous and competing pathways have to be considered in a simu-

lation of the selective reduction of NO by NH_2 radicals in the presence of various amounts of O_2 and CO as depicted in Fig. 10. Such model calculations can now be applied to realistic situations as shown in Fig. 11. Under this conditions one oberserves a very rapid reduction of NO at an optimum temperature. The model indicates that rapid mixing of NH_3 with the flue gases is essential for obtaining optimal reduction results. This can be achieved by using steam or other media for producing a high momentum of the injected material /28/. The main practical problem remaining, is the control of the ammonia injection level and location in a way that breakthrough of NH_3 is avoided under varying combustion conditions. This problem can be attacked by using laser methods for in situ monitoring of NH_3. Fig. 12 shows absolute absorption cross sections for NH_3 and NO lines at higher temperatures taken by a tunable diode laser sytem /28/. Using $^{13}CO_2$ in a wave guide CO_2-laser one observes coincidences between NH_3 and $^{13}CO_2$-laser lines in spectral regions where other components of the flue gas (H_2O, $^{12}CO_2$, SO_2, hydrocarbons) do not absorb significantly /32/. The $^{13}CO_2$ laser lines have a bandwidth of less than 0,01 cm^{-1} while the distance to the line centre of the NH_3-line is 0,02 cm^{-1} and the NH_3 line width is 0.08 cm^{-1}. By choosing a suitable reference line and an multipath absorption arrangement one can achieve a detection sensitivity of less than 1 vppm for in-situ measurements of NH_3-concentrations at higher temperatures by differential absorption with kHz repetition rates (see Fig. 13). The fast differential absorption technique eliminates problems arising from laser intensity variations as well as from other absorption and scattering processes in the flue gas.

B. Modelling of engine knock

Since more than hundred years /33/ one has observed that propagation of flames in a closed vessel can show a mode of combustion producing sharp pressure pulses associated with a characteristic sound effect. This was also realized as a major problem of the internal combustion engine /34-36/. Very early it became also clear that knocking must be closely connected with the chemistry of combustion. Application of CARS- and laser Raman-spectroscopy to knocking engines showed a fairly homogeneous distribution of the end-gas temperature around 1100 K /37/. Extension of the high temperature mechanism for the simulation of ignition and flame propagation in hydrocarbon/air mixtures to this temperature range allows the interpretation of auto-ignition processes on a chemical kinetic basis under conditions where turbulent

transport processes play a minor role /38/. The results explain the rapid grow of the radical pool by the chain-branching reaction sequence $HO_2 + RH \rightarrow H_2O_2 + R$, $H_2O_2 + M \rightarrow OH + OH + M$. At temperatures below 1000 K reactions of the type /39/ $R + O_2 \rightarrow RO_2$, $RO_2 + R'H \rightarrow ROOH + R'$, $ROOH \rightarrow OH + RO$ have to be taken into account. In calculations for realistic fuel (i-C_8H_{18}, n-C_7H_{16}) mixtures more than 160 species and 1300 reactions have to be considered /40/. As shown in Fig. 14 good agreement has been obtained between calculated and experimental determined knock-points /41/.

5. Laminar interaction of reactive and transport processes

A. Methane/air counter-flow diffusion flames

Laminar counter-flow diffusion flames constitute an important basis set for the simulation of turbulent combustion processes /42/. Having a library of pre-calculated "flamelets" at different strain rates and fuel/oxidizer mixture composition, the numerical treatment of turbulent flame structures with a "flamelet model" /43-45/ is reduced to a problem that can be solved within a reasonable amount of time on existing computers. Therefore, there is renewed interest in the study of diffusion flames under a variety of different burning condition to test and refine the validity of chemistry and transport properties used in modelling these flame structures. Among different types of counter-flow diffusion flames the configuration where the flame is established in the forward stagnation region of a cylindrical porous burner offers some inherent advantages. This type of diffusion flames - extensively studied by Tsuji and coworkers /46/ - are ideally suited for experimental work due to several reasons: Strain rates and mixture compositions can be adjusted easily, heat conduction problems are minimized because no rigid structures are in contact with the flame, and there is easy access to the flame front by intrusive and non-intrusive probing techniques. A schematic drawing of the burner configuration is shown in Fig. 15. A nearly 1-dimensional interaction of laminar flow and chemical reaction can be realized in this way.

Fuel and fuel/air mixtures - regulated by flow controllers - were ejected from a porous sintered brass cylinder (pore size of about 20 µm) glued to a water cooled cylindrical copper support of 40 mm diameter and a length of 100 mm. The burner was housed in a vertically oriented wind tunnel with a square cross section at the burner head of 100 x 100 mm. Air was blown up the

tunnel by four small fans or appropriate flow controllers (Tylan) depending on the volume flow needed. Swirl was reduced by the gas stream entering a settling chamber followed by a 100 mm long honeycomb plug-in, and turbulence by several grids mounted in the 250 x 250 mm rectangular flow channel before the gas entered the burner head through a converging nozzle. Hot wire measurements indicated an essentially flat profile of mean velocity in a plane perpendicular to the flow channel axis. Two micrometer screws enabled to move the burner head up and down relative to the fixed CARS laser beams. The laser beams entered the burner head parallel to the axis of the sinter cylinder through small holes (5 mm diameters) in the side walls.
Two beams emitted by a Nd-YAG-laser (Quanta Ray DCR1A) at 532 nm were used to pump a broadband dye-laser which delivered about 10 mJ at the Stokes shifted wavelength. The pump beams were achieved by sequentially doubling the fundamental and residual 1.06 µm output from the first frequency doubler. The secondary green beam was used to transversely pump the Stokes dye oscillator. A brewster plate polarizer ensured an output beam 90% vertically polarized. The dye-laser and part of the 532 nm pump beam (30 mJ) were collinearly combined in a USED-CARS phase matching geometry /47/. The CARS signal emerging from the measurement point (actually a cylinder approximately 60 µm in diamter and 1 mm long) was filtered off the residual pump and Stokes beams components and dispersed in a 1.3 m-monochromator (McPherson Mod. 209) equipped with a 2400 1/mm holographic grating. The linear dispersion in the plane of the intensified diode array camera (SI, Mod. IRY, 512 pixels) mounted behind a magnifying lens was measured to be 0,14 cm^{-1} per diode pixel. Throughout the experiments possible non-resonant CARS signal contributions complicating data evaluation /48/ were suppressed by polarization techniques /49/. Averaged spectra (typically 300 laser shots) were stored in a laboratory computer and transfered to a larger computer (IBM 3090-180) for further analysis.

Temperatures were deduced from computer generated least squares fitting spectral shapes of nitrogen vibrational-rotational Q-branch CARS spectra to measured spectra with temperature as a variable parameter. To get precise information on temperature from CARS spectra, a simulation program has to take into account collisional narrowing effects /50/. Another influence resulted from cross coherence effects induced by using multimode laser as a light source in generating CARS spectra. This phenomenon accounts for partial coherences in the CARS signals /51,52/. Cross coherence effects are mainly induced when correlated laser fields were used in generating CARS signals

which led to convolution procedures different from the classical descriptions given by Yuratich /53/. Following a procedure of Koszykowsky et al /54/, the temperature dependent part of the complex G-matrix was diagonalized. If the off-diagonal elements in the G-matrix - which describe the relaxation rates between states of different energy in the colliding molecule and therefore are responsible for collisional narrowing - were ignored, the previously used isolated line model results. In the current version of the fitting program routines were included which use the closed form solution of Greenhalgh and Hall /51/. For the fitting routine the procedure commonly used /55/ was replaced by orthogonal "Householder" transformations. To reflect the real measurement situation the distortion of the spectrum by the detector and spectrograph instrument functions as well as the pump laser linewidth had to be included in the simulation program by appropriate convolutions. Best results have been obtained by a priori fitting of these parameters to a CARS spectrum taken at room temperatures. Species concentrations were derived directly from the CARS signal intensity /56/.

For a quantitative treatment of the flame structure, the corresponding continuity equations for mass, y-direction momentum, energy, and chemical species in a laminar stagnation point flow had to be solved. They were discussed in detail in /57/.

These equations are:

2D-Continuity Equations

$$\frac{\partial}{\partial t}\rho + \frac{\partial}{\partial z}\rho u + \frac{\partial}{\partial y}\rho v = 0$$

$$\rho\frac{\partial \lambda}{\partial t} + \rho u\frac{\partial \lambda}{\partial z} + \rho v\frac{\partial \lambda}{\partial y} = u\frac{\partial p}{\partial z} - \frac{\partial}{\partial y}j_q$$

$$\rho\frac{\partial u}{\partial t} + \rho u\frac{\partial u}{\partial z} + \rho v\frac{\partial u}{\partial y} = -\frac{\partial p}{\partial z} + \frac{\partial}{\partial y}\left(\mu\frac{\partial u}{\partial y}\right)$$

$$\rho\frac{\partial \omega_i}{\partial t} + \rho u\frac{\partial \omega_i}{\partial z} + \rho v\frac{\partial \omega_i}{\partial y} = \frac{\partial}{\partial y}j_i + r_i$$

Fluxes

$$j_i = -D_i^M \rho\frac{\partial \omega_i}{\partial y} - D_i^T\frac{\partial \ln T}{\partial y}$$

$$j_q = -\frac{\lambda}{c_p}\frac{\partial \lambda}{\partial y} - \sum_i h_i j_i + \sum_i h_i\frac{\lambda}{c_p}\frac{\partial \omega_i}{\partial y}$$

Transformation

$$\eta = \sqrt{\frac{c}{(\rho\mu)_e}}\int_0^y \rho\, dy$$

Transport

$$D_i^M = \frac{1-\omega_i}{\sum_{j\neq i}\frac{x_j}{\mathcal{D}_{ij}}}$$

$$\lambda = \frac{1}{2}\left\{\sum_i x_i\lambda_i + \left(\sum_i \frac{x_i}{\lambda_i}\right)^{-1}\right\}$$

$$\mu = \frac{1}{2}\left\{\sum_i x_i\mu_i + \left(\sum_i \frac{x_i}{\mu_i}\right)^{-1}\right\}$$

c_p=specific heat capacity, h=specific enthalpy, r=mass scale chemical rate of formation, t=time, T=temperature, u=flow velocity in x-direction, w=mass fraction, x,y=cartesian space coordinates, =heat conductivity, p=pressure, μ=dynamic viscosity; index i stands for i^{th} chemical species of the system).

Use of the symmetry of the arrangement led to a set of ordinary differential equations depending on the spatial coordinates y and the time t only.
For the solution of these time dependent equations a finite differences method of second order in space and first order in time was used. The boundary conditions at the cylinder were

$$V = V_w \qquad f' = 0 \qquad T = T_w$$

$$w_{H,w} = 0 \qquad w_{H_2,w} = w_{H_2,u} - \frac{j_{H_2,w}}{V_w} - \frac{j_{H,w}}{V_w}$$

$$w_{i,w} = w_{i,u} - \frac{j_{i,w}}{V_w} \qquad i = 1,2,\ldots N$$

(index w denotes conditions at the cylinder, index u denotes of the unburned gas), and at the free stream side (index e)

$$j' = 1 \qquad T = T_e$$

$$w_i = w_{i,e} \qquad i = 1,2\ldots N$$

In addition, the code was modified to use the air velocity at a specified location on the free stream side as a second boundary condition if desired. For this purpose, the strain rate a was estimated as an eigenvalue of the system from the trivial differential equation

$$\frac{\partial a}{\partial y} = 0$$

because otherwise the problem would have been overdetermined. About 40 non-uniformly spreaded grid points for the non-premixed and about 70 grid points for the partially premixed case, with a distribution adapted to the steepness of the temperature profile, were used to span the coordinate system. The interpolation scheme used after regridding was changed compared with former versions of the code. A routine developed by Fritsch et al. /58/ based on monotone piecewise cubic interpolation was implemented. This resulted in less distortion of the profiles after regridding and reduced time steps necessary to get converged solutions.

For calculation of diffusion coefficients D_i^m, thermal diffusion coefficients D_i^T, heat conductivities λ, and dynamic viscosities μ, data were taken from molecular parameters. To calculate the transport parameters, a formula given by Hirschfelder et al. were used /59/. A simplified transport model was applied because comparison with multicomponent transport models led to errors relatively small if compared to those caused by uncertainties in the reaction mechanism /60/. If good experimental data for heat conductivity or diffusivity of species were available, those data were taken as basis for a fit. For all other species, transport properties were calculated from atomic or molecular parameters, respectively.

The reaction mechanism taken into consideration here consisted of more than 200 elementary steps (including reverse reactions) of about 30 species. The major components of this mechanism includes the H_2-O_2-system, CO oxidation, degradation of methane to CO, alkyl recombination to ethane, and propane, and consumption reactions of these higher hydrocarbons. Kinetic data were taken from /60/ with minor revisions due to new experimental results /61/. The rates for the reverse reactions were calculated with help of equilibrium constants derived from thermodynamical data.

In Fig. 16 temperature profiles measured by CARS in flames with velocity gradients $a=250s^{-1}$ and $350s^{-1}$ are shown together with the numerical results. The measured locations of the temperature maxima agree quite well with those of the calculated ones. The general shapes and widths of the profiles as measured with CARS are very similar to those of the calculated profiles while previous thermocouple measurements /46/ show significant discrepancies /57/. The computed peak temperatures in all cases are a little higher than those measured by CARS. This may be partly attributed to the fact that radiative losses are not included in the modeling calculations. Heat flux to the cylinder may be of increasing importance for higher velocity gradients. Similar results are obtained for concentration profiles (see Fig. 17).

However, as shown in Fig. 18a, for weakly strained flames important in 'flamelets' of technical turbulent diffusion flames larger deviations between simulated and measured temperatures are observed. For low values of the velocity gradient the thickness of the combustion zone becomes comparable or even larger than the boundary layer thickness. In the simulation a similarity solution has been employed which uses the boundary layer approximations and which is strictly valid only along the stagnation streamline. In particular, from the boundary layer approximations a too simplified, one-dimensional description of the pressure field result, which is unable to reflect real effects such as the modification of the pressure field due to apparatus effects or to the flame itself /57/. The pressure effects invalidate the boundary layer approach and necessitate a full numerical treatment of the two-dimensional pressure field. It is anticipated that a true two-dimensional computation of the flow field leads to prediction of a thicker combustion zone; in particular, the predicted steepness of the temperature profile at the freestream edge of the flame should then better be described. For the case of the partially premixed flames the agreement between calculated and measured temperature profiles is also less satisfactory than for the pure diffusion flame (see Fig. 18b). These flames consist of a premixed flame near the cylinder followed by a diffusion flame built of the fuel containing burnt gas of the premixed flame and the air stream. The slight temperature rise between the inner (premixed) and the outer (diffusion) type flame zone can be observed both in the experimental data and the numerical results. The measured widths of the flame zone are comparable with those of the calculated temperature profiles. However the locations of the measured and calculated temperature profiles differ substantially. Structure and position of pure diffusion flames are mainly

controlled by diffusion. The flame is always located at the plane of stoichiometric mixture. The influence of chemistry on its position is not as important as it is for premixed flames. The introduction of a premixed sub-flame into this diffusive structure results in an increasing complexity of the flame structure. A premixed flame with a stoichiometry of Φ =1.66 would not burn without the supporting outer diffusion flames because the flame is beyond the rich flammability limit of methane/air flames (about Φ =1.60). So the reaction mechanisms could not be properly tested for the pure premixed flames. The influence of the premixed sub-flame decreases by increasing Φ because the system becomes more similar to pure diffusion flames. The position of a premixed flame is very sensitive to the flame velocity which in turn depends strongly on chemistry. Minor problems with important reaction rates not properly determined may cause the shifts of the profiles as can be observed in the numerical results. Studies on premixed flames near to quenching reveal very strong dependence of their behaviour and structure on minimal changes in parameters of some elementary reactions. Future sensitivity studies on the reaction mechanism used here will allow an identification of important elementary reactions in this very fuel rich regime. This may lead to more satisfactory results for the position of partially premixed diffusion flames.

B. CO_2-laser induced ignition of O_3/O_2 mixtures in cylindrical cells

The experiments on laser ignition were performed with gas mixtures composed of ozone and oxygen, e.g. the ozone decomposition flame. Light absorption of O_3 was used to monitor flame propagation in the UV-spectral range as well as to initiate the reaction by absorption of CO_2-laser pulses in the IR spectral range. Hence there was no need for additional sensitizers (e.g. SF_6) to absorb the laser light, the simple chemistry of the O_2-O_3 system was preserved. Fig. 19 shows schematically the experimental set-up described in detail in /63,64/. Light pulses of a TEA CO_2-laser operating at = 9.552 µm in multimode oscillation were collimated to a beam waist of 2.7 mm width along the axis of a cylindrical vessel (diameter = 18 mm, length = 63 mm). The reaction was detected by UV light absorption on three paths perpendicular to the axis at the longitudinal positions = 12, 32 (exact image of a circular aperture irradiated by the laser), and 52 mm behind the entrance window.

Fig. 20 shows the light intensity at λ = 312.6 mm transmitted in a perpendicular detection paths (z = 32mm). The absorbed CO_2-laser energy causes a steep decrease of the UV-light intensity due to the high ro-vibrational excitation produced in the O_3 molecules. This excitation relaxes into the remaining degrees of freedom of the gas mixture. The relaxation is reflected in an increase of the signal. A new thermal equlibrium is attained in the irradiated region of the cell. The corresponding intensity level is slightly lower than that before the laser pulse since at λ = 312.6 nm, the O_3 absorption rises strongly with increasing temperature /65/.
It should furthermore be emphasized that the onset of the reaction is influenced by acoustic modes of the gas volume stimulated by the dissipation of the absorbed laser energy /64/. The corresponding intensity oscillations exhibit a period of 45 µsec, determined by the dimensions of the vessel. One clearly identifies the induction period when the flame starts to move into the volume not irradiated by the laser.

The ignition process is simulated mathematically by solving the corresponding system of conservation equations /66/. For one-dimensional geometries (infinite slab, infinite cylinder or sphere), after transformation into Lagrangian coordinates and using the uniform pressure assumption, these equations may be written as:

$$\rho c_p \frac{\partial T}{\partial t} - \frac{\partial P}{\partial t} = -\rho v c_p \frac{\partial T}{\partial r} - j_H c_p \frac{\partial T}{\partial r} + \frac{1}{r^n}\frac{\partial}{\partial r}\left(r^n \lambda \frac{\partial T}{\partial r}\right) - \sum_i r_i h_i$$

$$\frac{\partial \rho}{\partial t} = -\frac{1}{r^n}\frac{\partial (\rho v r^n)}{\partial r}$$

$$\rho \frac{\partial w_i}{\partial t} = -\rho v \frac{\partial w_i}{\partial r} - \frac{1}{r^n}\frac{\partial j_i}{\partial r} + r_i$$

$$\rho \frac{\partial v}{\partial t} = -\rho v \frac{\partial v}{\partial r} + \frac{\partial P}{\partial r} + \frac{\partial}{\partial r}\left(2\mu \frac{\partial v}{\partial r}\right) + \frac{2n\mu}{r}\left(\frac{\partial v}{\partial r} - \frac{v}{r}\right)$$

$$j_H = \frac{\sum c_{p,i} j_i}{c_p} \quad ; \quad j_i = -\rho D_{iM} \frac{\partial x_i}{\partial r} - D_{iT}\frac{1}{T}\frac{\partial T}{\partial r}$$

$$D_{iM} = \frac{1-w_i}{\sum_{j} x_j / D_{ij}} \quad ; \quad \lambda = 0.5 \left\{ \sum_i x_i \lambda_i + \left(\sum_i \frac{x_i}{\lambda_i}\right)^{-1} \right\}$$

with n = 0 for infinite slab, n = 1 for infinite cylinder, n = 2 for sphere, P is the pressure, T the temperature, t is the time, w_i the mass fraction of species i, M_i the molar mass of species i, r_i the molar rate of formation of species i, h_i the specific enthalpy of species i, $C_{p,i}$ the constant pressure heat capacity of species i, $D_{i,M}$ the diffusion coefficients of species i, D_{ij} binary diffusion coefficient, $D_{i,T}$ Thermodiffusion coefficient, ρ = the density M = molar mass, λ = thermal conductivity of the mixture, c_p = heat capacity of the mixture.

The term for the external energy source is given by

$$\dot{q} = \frac{\Delta}{r_s} \cdot \exp\left(-(r/r_s)^8\right) \qquad \text{for } 0 < t \leq t_s$$

$$\dot{q} = 0 \qquad \text{for } t > t_s$$

where r_s denotes the radius of the laser beam, t_s = source time and Δ = density of source energy. Spatial discretization using finite differences leads to a system of ordinary differential and algebraic equations which can be solved numerically. Due to the large ratio of vessel diameter to flame front thickness and to diameter of the artificial energy source adaptive gridding has to be used in case of ignition by artificial energy sources. Determination of the grid point density is done by equipartitioning the integral of a mesh function and inverse interpolation, the mesh function given by a weighted norm of temperature gradient and curvature. Piecewise monotone cubic Hermite interpolation is used for the static regridding /67-73/. The resulting systems of ordinary differential/algebraic equations can be solved using the computer codes DASSL /74/ or LIMEX /75,76/.

A typical simulation of ignition in an oxygen-ozone mixture is given in Fig. 21. After a relatively long induction period (confirming the corresponding experimental observation) there is a thermal explosion in the ignited gas pocket. This explosion initiates flame propagation across the vessel with subsequent equilibration by transport processes. Calculated minimum thermal ignition in energies are somewhat higher than experimental ones /77-79/. To get an idea of the ozone deflagration near to ignition limit linearized ignition diagrams have been determined without consideration of shot to shot fluctuations. They have been deduced from the periods passing until the start and the end of the reaction on the various probe beams and from the average longitudinal and radial velocities. Fig. 22 shows an example for the behaviour

near to the ignition limit. The deflagration starts and also proceeds slowly with a pronounced conical shape. In the case of higher fluence the flame front propagation usually becomes faster and nearly cylindrical symmetry is attained. Therefore, it is obvious that the behaviour of the macroscopic flame depends via the distribution of the laser heating in the beam waist region on the early processes of laser excitation and molecular relaxation. This feature is also important for the determination of the minimal ignition energy. The experiments accomplished so far revealed the existence of reproducible minimum of incoming as well as absorbed laser energy that brings about ignition for a given gas mixture. As a rough estimate for the ignition limit the beam waist-averaged energy density of absorbed laser energy was presented earlier /79/. These values are assumed to be a lower limit of the actual energy density in the ignition volume, i.e. the part of the beam waist region where energy release from laser absorption is a maximum. Clearly 2-dimensional calculations are needed in future to describe the situation near the ignition limit /78/.

6. Turbulent interaction of reactive and transport processes

In the majority of industrial combustion devices the characteristic dimensions and flow velocities are sufficiently large for the flow to be turbulent. Turbulent flows in combustion can be divided in two categories: premixed and non-premixed situations. Combustion in spark ignition engines occurs in the premixed mode while for safety reasons in most furnaces as well as gas turbines and diesel engines combustion takes place in a diffusion flame. The two categories exhibit quite different time-scales for convection, diffusion and reaction.

Besides direct simulations of turbulent chemically reacting flows, discrete vortex dynamics methods /81/ and numericals simulations of the evolution of probability density functions (pdf) /82,83/, several practical approaches exist to link chemical reactions to existing models of turbulent flow field predictions and to compute the turbulent mean values of the thermochemical variables. One approach is to solve model transport equations for the turbulent flow field and an additional scalar quantity /84/. The mean values of the other quantities of interest are then obtained by applying the earlier mentioned laminar flamelet model /42-45/. The laminar flamelet model is applicable to circumstances where "fast-chemistry" assumptions apply to the conversion of

the fuel so that combustion occurs in asymptotically thin layers ("flamelets") embedded within the turbulent flow field. In the case of premixed turbulent combustion packets of burned and unburned mixture are separated by the flamelet interfaces. The flamelets under these conditions have the structure of 1-dimensional strained laminar flames. The strain often decreases the rate of heat release in a flamelet and a large strain rate can cause extinction of the flamelet /85/. Detailed calculations of the structure and properties of strained and unstrained premixed laminar flames can be used to compile a "strained flamelet library" for subsequent use in turbulent flame calculations. A model for the distribution of the scalar and scalar dissipation in the turbulent flow have to be used /86,87/. Small turbulent length scales can generate a large flamelet area, e.g. wrinkled or ruptured laminar flames, which can result in rapid heat releas. On the other hand small scales may also have the opposite effect, since they are also associated with large strain rates and local extinction which results in a reduction in the heat release. Flamelet-models for premixed /84/ and non-premixed combustion /88-91/ have successfully been applied to various flames. Beside problems that are inherent in all approaches currently applied one has to take into account that flamelet models are applicable only if the length scales of turbulent eddies are large compared with the reaction-zone thickness of the flamelets. Another approach is to solve the averaged equations for the turbulent flow field and to look at certain fluid particles from a Langrangian point of view /92-94/. The chemical reaction rate of an individual fluid particle is derived from the instantaneous values of the respective thermochemical variables, these values being determinated by the "history" of the particle, that is its turbulent exchange of momentum and energy with other particles. A third approach is the solution of the averaged transport equations for the enthalpy of the mixture and the mass fraction of the chemical species. In the latter equations the chemical source terms must be modeled in a way that the chemistry-turbulence interaction occuring in the flow are described. Here often a direct-closure approach with a pdf-closure of the chemical production term is employed /91, 95, 96/.

In Fig. 24 axial and radial profiles of the mean temperature and the mean mass fractions of the major species in a turbulent CO/air diffusion flame obtained by the letter pdf-closure approach are compared with experimental data /97/. In Fig. 25 results from the direct closure approach are compared with calculations using the laminar flamelet model for the same flame. In both experiments and numerical simulations the fuel contained 3% H_2

to stabilize the flame on the nozzel rim. It is seen that the agreement with measured and computed profiles is generally good. One reason for the observed disagreement between computed and measured temperatures are the boundary conditions which are not unambiguously defined in /97/. Furthermore the temperature has been measured by unshielded thermocouples. A significant breakthrough of oxygen is predicted on the axis, compare Fig. 24, a result that indicates that the flame is lifted from the burner port. The experimental conditions, however, are such that the strain of the laminar flamelet is comparatively small so that actually only the unstrained laminar flamelet represents the ensemble of laminar diffusion flamelets. Further experiments should therefore concentrate on flames with much higher Reynolds numbers. In addition, as illustrated in Fig. 26, information on the correlation at temperature and species concentration is required to obtain a more clear picture about the limits of applicability of the different models /106,107/.

Various methods for imaging of combustion and flow processes using dopants have been described. Some of these are based on the seeding of particles into the flow to be investigated. For example, $TiCl_4$ added to the combustion chamber reacts with water formed in the flame front to form TiO_2 particles, which can serve as centres for Mie scattering /99/ and can be used for 2D-visualization. However, such methods involve complex data processing and are not always applicable (e.g. due to particle lag). These limitations can be largely overcome by seeding with molecular fluorescent dopants such as CO (2-photon excitation) /100/, NO /101/, NO_2 /102/, I_2 /103/, biacetyl /104/, and organic exciplexes /105/ for imaging, although it should be remembered that each type of dopant is only suitable for certain applications. As shown in Fig. 27 the intensity of the fluorescence signal can be expressed by the spectroscopic parameters, the ground state population and the electronic quenching rate (Q) /108/. Since at atmospheric and higher pressures, fluorescence lifetimes (equivalent to 1/Q,) for many key species in combustion are on the order of nanoseconds or less, an ultrashort-pulse laser coupled with fast detection and data acquisition/processing is required for direct measurements. Such time-resolved measurements were made with a home-built picosecond dye laser (Fig. 28).

Using an excimer pump laser (308 nm, EMG MSC 103 Lambda Physik). The starting pulse length of 8 ns was shortened first in a quenched transient dye laser (QDTL), which operates by suppressing resonator transients in a double

resonator system /109/. After amplification, these pulses were used to pump the oscillator of the second stage, the distributed feedback laser (DFDL) /110/. In the DFDL, feedback is provided by Bragg scattering from spatially periodic perturbations of the optical gain and pulse shortening achieved by spatial separation of the first resonator peak from the following peaks. For OH(A-X) excitation, rhodamine B was used in the DFDL cuvette. The second harmonic of the laser frequency was generated by passing the beam through an 8 mm long crystal of β-BaB_2O_4. The laser beam was directed into an atmospheric pressure, water-cooled (thermostat 50°C) burner of the flat-flame type. Premixed flows of methane/ air were supplied to the burner using Tylan mass flow controllers. Integrated fluorescence from the OH radicals was observed at right angles to the focussed laser beam. Fluorescence light was focussed onto the 100 µm x 15 mm slit of a streak camera (C1587 Hamamatsu, S-20 photocathode). The data were interpreted by a temporal analyzer (Hamamatsu C2200).

Measurements of the OH(A-X) lifetime at the $Q_1 5$ line at 308.52 nm were made at different heights above the burner surface, i.e. from 0.5 to 20 mm, also with a constant height of 20 mm but varying ϕ from 0.77 to 1.43 /111/. Within experimental error, no change in lifetime could be discerned in either series of measurements (see Fig. 29). The experimental result, that the collisional quenching rate is nearly constant throughout an atmospheric pressure flame although for different mixing ratios simplifies the determination of absolute number densities in such flames.

Another way to avoid the complications caused by quenching processes in LIF spectroscopy is to work with fluorescent molecular states with very short lifetimes due to fast predissociation processes /108,113/. Experiments using acetaldehyde as dopant with short radiation lifetime for flame front visualization will be described here. Detailed investigations on LIF of acetaldehyde in supersonic jets /114/ have provided information on the rovibronic levels of the S_1 state below the photodissociation threshold together with lifetimes for many of these levels and a more reliable value for the origin of the S_1 state. The conclusion of studies was, that the dominant relaxation process from lower vibrational levels of S_1 acetaldehyde is irreversible internal conversion to S_0 /115/. Studies of the dependence of acetaldehyde fluorescence on added gas pressures up to 25 bar establish that this molecule is a suitable tracer to show up the flame front also in combustion at higher pressures /116/. Imaging of laminar and turbulent combustion processes was realised using the set-up shown in Fig. 30.

The combustion device (supplied by Daimler-Benz) has a square cross section piston to allow easy access for line-of-sight measurements /117/. The laser light sheet (dimensions 25 mm x 75 µm) entered the combustion chamber through the quartz side window. The LIF-signals from acetaldehyde and OH radicals were collected through the top window by different imaging optics (Nikon 1:1.2/50 and 1:4.5/105 mm) of the image-intensified CCD-camera (Proxitronic Nanocam, gate time 25 ns). Fluorescence images were digitized and processed by a frame grabber (MATROX MVP-AT) and connected to a personal computer (ZenithΔ T386). Images were then taken at different times after ignition (Fig. 31b), using a detection region of approximately 10 x 20 mm. OH radicals were excited with the XeCl-excimer laser (EMG 150 EST, Lambda Physik) operating in the tunable mode (FWHM $1cm^{-1}$), tuning range 307,8 to 308,5 nm. This wavelength region corresponds to the $OH(X^2\Pi\text{-}A^2\Sigma^+, 0,0)$ vibronic transition. The linewidth of a rotational line of this transition at detection pressures (5-15 bar) and 2400 K is approximately 1.5 cm^{-1} so that only one or two rovibronic transitions of OH can be excited. Also, calculations /110/ have shown that for a number of rotational levels $N'' < 10$ above 2000K, the proportionally factor between the fluorescence signal and absorbing species number density is constant within about 10%.

A direct comparison of the two flame front visualization techniques using OH and acetaldehyde fluorescence is shown first for laminar burning conditions. In this case the combustion engine was used as a simple combustion chamber only with the piston fixed at BDC. The acetaldehyde image (Fig. 31b) is the negative of the OH image (Fig. 31a), since OH fluoresces in the burned acetaldehyde in the unburned region. The images were taken at the same time after ignition and show that the burned regions have the same size. This means that the flame front velocities are equal and hence that small acetaldehyde concentrations in the fuel do not affect the flame propagation. The boundary between the burned and unburned zones can easily be recognized. Only a small zone with an intermediate concentration of the gas mixture can be seen between the unburned and burned regions.
Fig.32 was taken with the piston moving showing now turbulent flame fronts. The OH-line intensity profiles (Fig. 32a) can, in principle, be used to estimate the thickness of the turbulent flame front by determing the shortest distance from zero to maximum fluorescence signal. However, since the angle at which the laser beam crosses the flame is unknown, only an upper limit can be given. In this case a flame front thickness of 300 $\pm$ 70µm is obtained.

The combustion regime in the engine corresponds to the flamelet region of the Borghi diagram (s. Fig. 26). The packets of burned and unburned mixture separated by the flamelet interfaces can be seen in both pictures. The OH radical fluorescence allows also detection of flame quenching at lean mixtures. In the case of λ = air/fuel ratio = 1 the flame propagates well towards the cylindar walls, whereas for λ = 1,5 the flame front stagnates. The flame front quenching can be seen clearly in Fig. 33 by a disappearing reaction zone in the main parts of the image. Only inlets, which have a concave curvature, burned well. This can be understood because a convex reaction zone has a higher portion of its surface inside the cold unburned fuel than a concave structure, resulting in a higher degree of heat loss and therefore poorer burning behaviour compared to concave structures. Particularly at early detection times, where the inlet structures burned much better than the outlets, the inlets burn away with increasing time whereas the outlets more or less stagnate due to their relatively poor burning behaviour. This eventually results in a reduction in the number of inlets and smooths the flame front.

References

/1/ J. Warnatz, Ber. Bunsenges. Phys. Chem.87, 1008(1983)

/2/ J. Wolfrum, 20th Symp.(Int.) on Combustion, p. 559, The Combustion Institute (1984)

/3/ K. Kleinermanns, J. Wolfrum, J. Chem. Phys.80, 1446 (1984)
E. Linnebach, K. Kleinermanns (to be published)

/4/ K. Kleinermanns, R. Schinke, J. Chem. Phys. 80, 1440 (1984)

/5/ K. Kleinermanns, E. Linnebach, Appl. Phys. B36, 203 (1985)

/6/ I. Schechter, R.D. Levine, Faraday Discussion 84, paper 10 (1987)

/7/ J.A. Miller, J. Chem. Phys. 74, 5120 (1981)

/8/ C.F. Melius, R.J. Blint, Chem. Phys. Lett. 64, 183 (1979)

/9/ C. Cobos, H. Hippler, J. Troe, J. Phys. Chem. 89, 342 (1985)
J. Troe, J. Phys. Chem. 90, 3485 (1986)
J. Troe, Combust. Flame (1988: in press)

/10/ T.H. Dunning, Jr., S.P. Walch, M.M. Goodgame, J. Chem. Phys. 74, 3482 (1981)
G.J. Vazquez, S.G. Peyerimhoff, R.J. Buenker, Chem. Phys. 99, 239 (1985)

/11/ A.J.C. Varandas, J.Brandas, L.A.M. Quintales, J. Phys. Chem. 92, 3732 (1988)

/12/ G.L. Schott, Combust. Flame 21, 357 (1973)

/13/ Th. Just, P. Frank, Ber. Bunsenges. Phys. Chem. 89,181 (1985)

/14/ A.N. Pirraglia, J.V. Michael, J.W. Sutherland, R.B. Klemm, J.Phys. Chem. (1988, in press)

/15/ B. Fritz, K. Lorenz, W. Steinert, R. Zellner, Oxidation Communications 6, 363 (1984)

/16/ B.S. Haynes, Combust.Flame 28, 113 (1977)

/17/ A. Szekely, R. Hanson, C.T. Bowman, Int. J. Chem. Kin. 16, 1609 (1984)

/18/ A. Jacobs, M. Wahl, R. Weller, J. Wolfrum, Chem. Phys. Lett. 144, 203 (1988)

/19/ J.A. Miller, C.F. Melius, 21st Symp. (Int.) on Combustion p. 919, The Combustion Institute (1986)

/20/ M. Gehring, K. Hoyermann, H. Schacke, J. Wolfrum 14th Symp. (Int.) on Combustion, p. 99, The Combustion Institute (1973)

/21/ J.S. Silver, C. Kolb, J. Phys. Chem. 86, 3240 (1982); 91, 3713 (1987)

/22/ P. Andresen, K. Kleinermanns, A. Jacobs, J. Wolfrum, 19th Sym. (Int.) on Combustion p. 11, The Combustion Institute (1982)

/23/ L.J. Stief, W.B. Brobst, D.F. Nava, R. Borkowski, J.V. Michael, J. Chem. Soc. Far. Trans. II 78, 1391 (1982)

/24/ J.L. Hall, D. Zeitz, J. Kasper, G.P. Glass, R.F. Curl, F.K. Tittel J. Phys. Chem. 90, 2501 (1986)

/25/ D.A. Dolson, J. Phys. Chem. 90, 6714 (1986)

/26/ R. Weller, J. Wolfrum, Periodic Report of the EC Energy Conservation Programme EN 3F-0092 (1986,1988)

/27/ J.A. Miller, M.C. Branch, R.J. Kee Combust. Flame 43, 81 (1981)
M.A. Kimmball-Linne, R.K. Hanson Combust. Flame 64, 337 (1986)
P. Glarborg, J.A. Miller, R.J. Kee, Comb. Flame 65, 177 (1986)

/28/ H. Hemberger, H. Neckel, J. Wolfrum, 3. TECFLAM-Seminar p. 47 ISBN3-926751-05-3 (1988)

/29/ R.K. Lyon U.S. Patent No. 3900.554

/30/ C.F. Melius, J.S. Binkley, 20th Symp. (Int.) on Combustion, p. 575, The Combustion Institute (1984)

/31/ Th. Dreier, J. Wolfrum, 20th Symp. (Int.) on Combustion p. 695, The Combustion Institute (1984)

/32/ A. Stein, B. Perry, D. Todd, Appl. Opt. 22, 3378 (1983)
B. Perry, A. Stein, US Patent 4,471,220

/33/ E. Mallard and H. Le Chatelier, Annals des Mines 8, 274 (1883)

/34/ W. Nernst, Zeitschrift Deutscher Ingenieur 49, 1426 (1905)

/35/ W. Jost, Explosions- und Verbrennungsvorgänge, Steinkopf, Darmstadt (1939)

/36/ A.K. Oppenheim, SAE paper 84-1339 (1984)

/37/ J.R. Smith, R.M. Green, C.K. Westbrook, W.J. Pitts, 20th Symp. (Int.) on Combustion, p.91, The Combustion Institute (1984)

/38/ C. Esser, U. Maas, J. Warnatz, SAEJ Proceedings, p. 335 (1985)
VDI-Berichte 574, 269 (1985)

/39/ M.P. Halstead, L.J. Kirsch, A. Prothero, C.P. Quinn, Proc. Roy. Soc. A346, 515 (1975)

/40/ J. Warnatz, C.K. Westbrook, 22nd Symp.(Int.) on Combustion, The Combustion Institute (1988)

/41/ A. Duoaud, G. de Soete (personal communication to J. Warnatz)

/42/ G. Damköhler, Z. Elektrochem. 46, 601 (1940)

/43/ F.A. Williams in Turbulent Mixing in Nonreactive and Reactive Flows (S.N.B. Murphy Ed.) p.189, Plenum (1975)

/44/ K.N.C. Bray, P.A. Libby, Phys. Fluids 19,1687 (1976)

/45/ N. Peters, Progr. Energy Combust. Sci, 10, 319 (1984)

/46/ H. Tsuji, Progr. Energy Combust. Sci. 8, 93 (1982)

/47/ A.C. Eckbreth, G.M. Pobbs, J.H. Stufflebeam, P.A. Tellex, Appl. Opt. 23, 1328 (1984)

/48/ R.J. Hall, L.R. Boedeker, Appl. Opt. 23, 1340 (1984)

/49/ L.A. Rahn, L.J. Zych, F.L. Mattern, Opt. Comm. 30, 249 (1979)

/50/ J.R. Hall, J.F. Verdieck, A.C. Eckbreth, Opt. Comm. 35, 69 (1980)

/51/ D.A. Greenhalgh, R.J. Hall, Opt. Comm. 57, 125 (1986)

/52/ R.E. Treets, Opt. Lett. 19, 226 (1984)

/53/ M.A. Yuratich, Mol. Phys. 38, 625 (1979)

/54/ M.H. Koszykowsky, R.L. Farrow, R. E. Palmer, Opt. Lett.10, 478 (1985)

/55/ A. Kim, J. Chem. Education 47, 120 (1970)

/56/ Th. Dreier, B. Lange, J. Wolfrum, M. Zahn, Appl. Phys. B45, 181 (1988)

/57/ G. Dixon-Lewis, T. David, P.H. Gaskell, S. Fukutani, H. Jinno, J.A. Miller, R.J. Kee, M.D. Smooke, N. Peters, E. Effelsberg, J. Warnatz, F. Behrendt, 20th Symp. (Int.) on Combustion, p. 1893, The Combustion Institute (1984)

/58/ F.N. Fritsch, J. Butland, LLNL preprint UCLE-87559(1982)

/59/ J.O. Hirschfelder, C.F. Curtiss, R.B. Bird, Molecular Theory of Gases and Liquids, Wiley, New York (1954)

/60/ J. Warnatz, Rate Coefficients in the C/H/O-System, in "Combustion Chemistry" (W.C. Gardiner, Jr., Ed.), Springer, New York (1985)

/61/ C. Esser, J. Warnatz, Progr. Energy Combust. Sci. (1988, to be published)

/62/ T. Dreier, B. Lange, J. Wolfrum, M. Zahn, F. Behrendt, J. Warnatz, Ber. Bunsenges. Phys. Chem.90, 1010 (1986)

/63/ B. Raffel, J. Warnatz, J. Wolfrum, Appl.Phys. B37, 189 (1985)

/64/ B. Raffel, J. Wolfrum, Ber. Bunsenges. Phys. Chem. 90, 997 (1986)

/65/ D.C. Astholz, A.E. Croce, J. Troe, J. Phys. Chem. 86, 696 (1982)

/66/ B. Raffel, J. Warnatz, H. Wolff, J. Wolfrum, R.J. Kee, in: Dynamics of Reactive Systems II, (J.R. Bowen, J.-C. Leyer, R.I. Soloukhin Eds.), p. 335. AIAA, New York (1986)

/67/ R.J. Kee, J. Warnatz, J.A. Miller, "A Fortran Program Computer Code for the Evaluation of Gas-Phase Viscosities Conductivities and Diffusion Coefficients". SANDIA Report SAND83-8209 (1983)

/68/ R.J. Kee, G. Dixon-Lewis, J. Warnatz, M.E. Coltrin, J.A. Miller, "A Fortran Computer Code for the Evaluation of Gas-Phase Multicomponent Transport Properties". SANDIA Report SAND86-8246 (1986)

/69/ J. Warnatz, Ber. Bunsenges. Phys. Chem. 82, 193 (1978)

/70/ N. Peters, J. Warnatz (Eds.), Numerical Methods in Laminar Flame Propagation. Vieweg. Braurschweig (1982)

/71/ F.N. Fritsch, J. Butland, J. Sci. Stat. Comput. 5, 300 (1984)

/72/ K.H. Ebert, P. Deuflhard, W. Jäger (Eds.), Modelling of Chemical Reaction Systems. Springer, Heidelberg (1981)

/73/ J. Warnatz, W. Jäger (Eds.). Complex Chemical Reaction Systems: Mathematical Modelling and Simulation. Springer, Heidelberg (1987)

/74/ L.R. Petzold, A Description of DASSL: A Differential/Algebraic System Solver, Sandia Report SAND82-8637. Sandia National Laboratories, Livermore (1982); IMACS World Congress, Montreal (1982)

/75/ P. Deuflhard, E. Hairer, J. Zugck, One-Step and Extrapolation Methods for Differential/Algebraic Systems. Univ. Heidelberg, SFB 123: Tech. Rep. 318 (1985)

/76/ P. Deuflhard, U. Nowak, Extrapolation Integrators for Quasi-Linear Implicit ODEs. Univ. Heidelberg, SFB 123: Tech. Rep. 332 (1985)

/77/ F.J. Weinberg, J. R. Wilson, Proc. Roy. Soc. A321, 41 (1971)

/78/ U. Maas, J. Warnatz, Combust. Flame (1988, to be published)

/79/ U. Maas, B. Raffel, J. Warnatz, J. Wolfrum, 21st Symp. (Int.) on Combustion p. 1869, The Combustion Insitute (1986)

/80/ B. Raffel, J. Wolfrum. Z. Phys. Chem. N.F. (1988, in press)

/81/ W.T. Ashurst, P.K. Barr, Combust. Sci. and Tech. 34, 227 (1983)

/82/ E.E. O'Brian in P.A. Libby, F.A. Williams (Eds.), Turbulent Reacting Flows, p. 185, Springer/Berlin, (1980)

/83/ S.B. Pope, Prog. Energy Combust. Sci. 11, 119 (1985)

/84/ N. Peters, 21st Symp. (Int.) on Combustion p. 1231, The Combustion Institute (1986)

/85/ K.N.C. Bray in: Complex Chemical Reaction Systems: Mathematical Modelling and Simulation (J.Warnatz, W. Jäger Eds.) p.356, Springer, Heidelberg (1987)

/86/ K.N.C. Bray, P.A. Libby, J.B. Moss, Combust. Sci. and Tech. 41, 143 (1984)

/87/ K.N.C. Bray, P.A. Libby, Combust. Sci. and Tech. 47, 253 (1986)

/88/ S.K. Liew, K.N.C. Bray, J.B. Moss, Combust. Flame 56, 199 (1984)

/89/ B. Rogg, F. Behrendt, J. Warnatz, 21st Symp. (Int.) on Combustion p. 1533, The Combustion Institute (1986)

/90/ B. Rogg, F. Behrendt, J. Warnatz, Ber. Bunsenges. Phys. Chem. 90, 1005 (1986)

/91/ F. Behrendt, H. Bockhorn, B. Rogg, J. Warnatz
in: Complex Chemical Reaction Sytem: Mathematical Modelling and Simulation (J. Warnatz, W. Jäger Eds.) p. 376, Springer, Heidelberg (1987)

/92/ A.S.C. Ma, D.B. Spalding, R.L.T. Sun, 19th Symp. (Int.) on Combustion, p. 393, The Combustion Institute (1982)

/93/ R. Borghi, E. Pourbaix, Physicochemical Hydrodynamics 2, 65 (1981)

/94/ R. Borghi, M. Gonzalez, Combust. Flame 63, 239 (1986)

/95/ R.W. Bilger in Turbulent Reacting Flows (P.A. Libby, F.A. Williams Eds.), p. 65 Springer, Berlin (1980)

/96/ H. Bockhorn in Mathematical Modeling in Combustion and Related Topics, (C.M. Braunner and C. Schmidt-Lainé, Eds.), p. 412. Martinus Nijhoff Publishers, Dordrecht (1988)
H. Bockhorn, 22nd Symp. (Int.) on Combustion, in press (1988)

/97/ M.K. Razdan, J.G. Stevens, Combust. Flame 59, 289 (1985)

/98/ M.C. Drake, R.W. Pitz, M. Lapp, C.P. Fenimore, R.P. Lucht, D.W. Sweeney, N.M. Laurendeau, 20th Symp. (Int.) on Combustion, p. 327, The Combustion Institute (1984)

/99/ L.D. Chen and W.M. Roquemore, Combust. Flame 66, 81 (1986)

/100/ J. Haumann, J.M. Seitzman and R.K. Hanson, Opt. Lett. 11, 776 (1986)

/101/ J.M. Seitzman, G. Kychakoff and R.K. Hanson, Opt. Lett. 10, 439 (1985)
G. Kychakoff, K. Knapp, R.D. Howe and R.K. Hanson, AIAA Journal 22, 153(1984)

/102/ R.J. Cattolica, 21st Symp. (Int.) on Combustion p. 1551, The Combustion Institute (1986)

/103/ B. Hiller and R.K. Hanson, Opt. Lett. 10, 206 (1985)

/104/ F. Itoh, G. Kychakoff and R.K. Hanson, J. Vac. Sci. Technol. B3, 1600 (1985)
B. Hiller, R.A. Booman and R.K. Hanson, Rev. Sci. Instr. 55, 1964 (1984)

/105/ L.A. Melton, J.F. Verdieck, Combust. Sci. Tech. 42, 217 (1985)
H.E. Cosage and L.A. Melton, Appl. Opt. 26, 2256 (1987)

/106/ R. Borghi in Recent Advances in Aeronautical Science (C. Buro, C. Casci, Eds.) Pergamon, London (1984)

/107/ J. Warnatz, 2. TECFLAM-Seminar (ISBN 3-926751-04-4), p. 7, Stuttgart (1986)

/108/ R.K. Hanson, 21st Symp. (Int.) on Combustion p. 1677, The Combustion Institute (1986)

/109/ Z. Bor, B. Racz, Appl. Opt. 24, 1910 (1985)
F.P. Schäfer, Laser und Optoelektronik, Nr. 2 (1984) p. 95

/110/ Z. Bor, IEEE J. Quant. Electrn. 16, 517 (1980);
A. Müller and Z. Bor, Laser und Optoelektronik Nr. 3 (1984) p. 187

/111/ R. Schwarzwald, P. Monkhouse, J. Wolfrum, Chem. Phys. Lett. 142, 15 (1987)

/112/ H.M. Hertz, M. Alden Appl. Phys. B42, 97 (1987)

/113/ P. Andresen, A. Bath, H.W. Lulf Appl. Optics 27, 365 (1988)

/114/ M. Noble and E.K.C. Lee, J. Phys. Chem. 87, 4360 (1983);
M. Noble, E.C. Apel and E.K.C. Lee, J. Chem. Phys. 78, 2219 (1983);
M. Noble and E.K.C. Lee,J. Chem. Phys. 80, 134, 81, 1632 (1984)

/115/ C.B. Moore and J.C. Weisshar, Ann. Rev. Phys. Chem. 34, 525 (1983)

/116/ H. Becker, K. Kleinermanns, P. Monkhouse, R. Suntz, J. Wolfrum, J. Koehler, G. Ziegler, Periodic Report of the EC Energy Conservation Programme EN3E-0056-D (1987)

/117/ R. Suntz, H. Becker, P. Monkhouse, J. Wolfrum, Appl. Phys. B47, 1-7 (1988)

/118/ G. Kychakoff, R.D. Howe, Appl. Opt. 23, 704 (1984)

Figure Captions

Fig. 1: Theoretical and experimental analysis of complex combustion systems

Fig. 2: Production of fast hydrogen atoms by Excimer laser photolysis and product detection by laser induced fluorescence

Fig. 3: Experimental arrangement for the study of reactions with translationally hot atoms and radicals by combination of excimer laser photolysis and LIF product detection

Fig. 4a: Nascent rotational state distribution of OH(v=0) formed in the reaction $H + O_2 \rightarrow OH + O$ at different collision energies (E_T) /3/. QCTC: Quasi Classical Trajectory Calculations /4/.

Fig. 4b: Fine structure state populations of OH formed in reaction (1) by hydrogen atoms with 1.84 eV relative translational energy (E_T)

Fig. 4c: Vector properties of reaction (1) (see text)

Fig. 5: Calculated and measured thermal rate constants for the reaction $H + O_2 \rightarrow OH + O$
Ref.: — Schott /12/, ● Just, Frank /13/, ▲ Pirraglia et. al. /14/, □ Miller /7/

Fig. 6: Elementary steps in the conversion of fuel-nitrogen to nitric oxide

Fig. 7: Experimental set-up for kinetic measurements at different temperatures using Excimer laser photolysis combined with laser-induced fluorescence detection /18/

Fig. 8a: Arrhenius diagram for reaction (-2)
Bowman et. al. /17/, Jacobs et. al. /18/

Fig. 8b: Arrhenius diagram for reaction (2)
Ref.: Bowman et. al. /17/, Haynes /16/, Fritz et. al. /15/, Jacobs et. al. /18/, Miller, Melius /19/

Fig. 9: Elementary steps in the selective reduction of NO by NH_2-radicals H_2O^* (ν:) vibrational excited water molecules

Fig.10a,b: Modeling of the selective reduction of NO with NH_3 in the presence of various amounts of CO and O_2 /28/.

Fig.11: Concentration-time profiles in the selective reduction of NO with NH_3 in a coal power plant /28,29/.

Fig.12: Temperature dependence of absolute IR-absorption coefficients of NO and NH_3 measured with a high resolution diode laser spectrometer /28/.

Fig.13: In-situ measurement of NH_3 concentrations by differential absorption

Fig.14: Measured /41/ and calculated /40/ auto-ignition behaviour in an engine fueled with i-C_8H_{18}

Fig.15: Experimental arrangement for measuring temperature and concentration profiles in a counter-flow diffusion flame with broadband USED-CARS /47,56/

Fig.16: Temperature profiles calculated (lines) and measured by CARS (□) in CH_4/air counter-flow diffusions flames with different strain rates

Fig.17: Comparison of calculations and CARS measurements for concentration profiles through the flame front of CH_4/air counter-flow diffusion flames /62/.

Fig.18: Calculated and measured (□ N_2, ▲ O_2) temperature profiles in counter-flow diffusion flames with a very low strain rate (a) and in a partially premixed flame with a = 62 s^{-1} and Φ = 1.66 (b)

Fig.19: Experimental set-up for the investigation of CO_2-laser induced ignition of O_3/O_2 mixtures

Fig.20: Transient signal of transmitted UV intensity (λ = 313 nm) perpendicular to the CO_2-laser direction (s. Fig. 19) of an O_2/O_3-mixture of P_{tot} = 0.35 bar with 20% O_3 following exposure to a CO_2 laser pulse of F_{in} = 0.97 J/cm^2

Fig.21: Example of the numerical simulation of a cylindrical ozone explosion p_{tot} = 0.35 bar, 20% O_3, E = 0.11 J/cm^3

Fig.22: Evolution of the CO_2-laser induced ozone decomposition flame near to ignition limit (hatched region = burned gas) /80/

Fig.23: Calculated pressure (a) and temperature (b) profiles in an igniting hydrogen-oxygen mixture (stoichiometric); cylindrical geometry, P = 1 bar, t_{ign} = 1ms, r_{ign} = 1mm, E_{ign} = 4J /78/

Fig.24: Axial and radial profiles of mean temperatures and mean mass fractions of major species for a carbon monoxide air diffusion flame. Solid lines represent numerical results /89/ symbols represent measurements reported by Razdan and Stevens /97/.

Fig.25: Mass fractions and temperature on the centerline of a turbulent carbon monoxide-air diffusion flame. Symbols are experimental data taken from Razdan and Stevens /97/. Solid lines: numerical results obtained from flamelet-model (a) and pdf-method (b) /89,90/

Fig.26: Borghi-Diagram describing different situations for the interaction of chemical reactions with turbulent flow fields /106,107/

v_f = Laminar flame velocity

l_f = laminar flame front thickness

v' = turbulent velocity

l_t = turbulent length scale

l_k = Kolmogorov length

Re_t = turbulent Reynolds number

Da = Damköhler number

Ka = Karlovitz number

Fig.27: Principles of laser induced fluorescence spectroscopy /108/

Fig.28: Experimental set-up for fluorescence life time measurements in atmospheric pressure flames DFDL (distributed feedback dye laser) QTDL (quench transient dye laser) SHG (second harmonic generation)

Fig.29: Lifetime measurements of OH excited at 308,52 nm ($Q_1$5 line) at various heights in a laminar premixed methan-air flame at atmospheric pressure

Fig.30: Experimental set-up for flame front imaging in an internal combustion engine /117/

Fig.31: Visualization of a laminar flame front in the set-up shown in Fig. 30 using laser induced fluorescence from OH radicals (a) and acetaldehyde (b)

(a) λ = air-fuel ratio = 1,0
d = distance cylinder head to light-sheet = 13mm
t_N = detection time after ignition = 10msec
P_N = detection pressure = 1,3 bar

(b) λ = 1,0
d = 13mm
t_N = 10msec
P_N = 1,5 bar

Position of the spark plug: midpoint of the combustion chamber (Fig. 30)

Fig.32: Imaging of the turbulent flame front in an internal combustion engine using OH-radical (a) and acetaldehyde (b) fluorescence

(a) λ = 1,4
d = 10mm
t_N = 11msec
P_N = 5,6 bar

Spark plug at the edge of the detection region

(b) λ = 1,0
d = 13mm
t_N = 6msec
P_N = 6,2 bar

Spark plug: midpoint of combustion chamber

Fig.33: Visualization of flame quenching in an internal combustion engine using OH radical fluorescence

(a) λ = 1,0
d = 13mm
t_N = 7msec
P_N = 4,4 bar

(b) λ = 1,5
d = 13mm
t_N = 21,5 msec
P_N = 1,5 bar

Spark plug at the edge of the detection region

Acknowledgement

I would like to thank Professor J. Warnatz for numerous interesting and stimulating discussions on the modeling of combustion systems.

The support of this work by the BMFT (TECFLAM), DFG (SFB 123), Stiftung Volkswagenwerk, Fonds der Chemischen Industrie and the Comission of the European Communities is gratefully achnowledged.

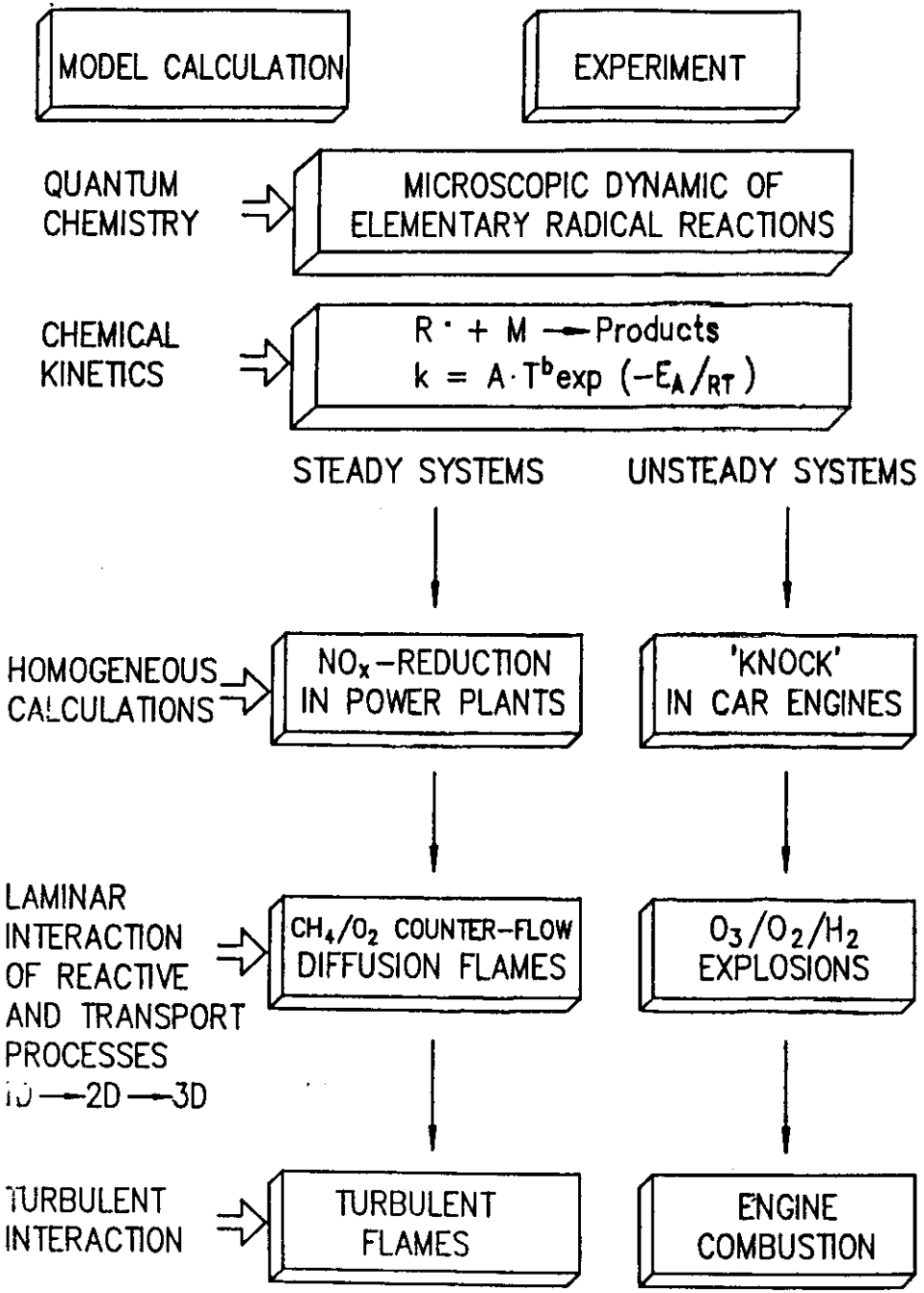
MODEL CALCULATION
EXPERIMENT
QUANTUM CHEMISTRY
MICROSCOPIC DYNAMIC OF ELEMENTARY RADICAL REACTIONS
CHEMICAL KINETICS
R · + M → Products
k = A · T^b exp (−E_A/RT)
STEADY SYSTEMS
UNSTEADY SYSTEMS
HOMOGENEOUS CALCULATIONS
NOx−REDUCTION IN POWER PLANTS
'KNOCK' IN CAR ENGINES
LAMINAR INTERACTION OF REACTIVE AND TRANSPORT PROCESSES
1D → 2D → 3D
CH4/O2 COUNTER-FLOW DIFFUSION FLAMES
O3/O2/H2 EXPLOSIONS
TURBULENT INTERACTION
TURBULENT FLAMES
ENGINE COMBUSTION

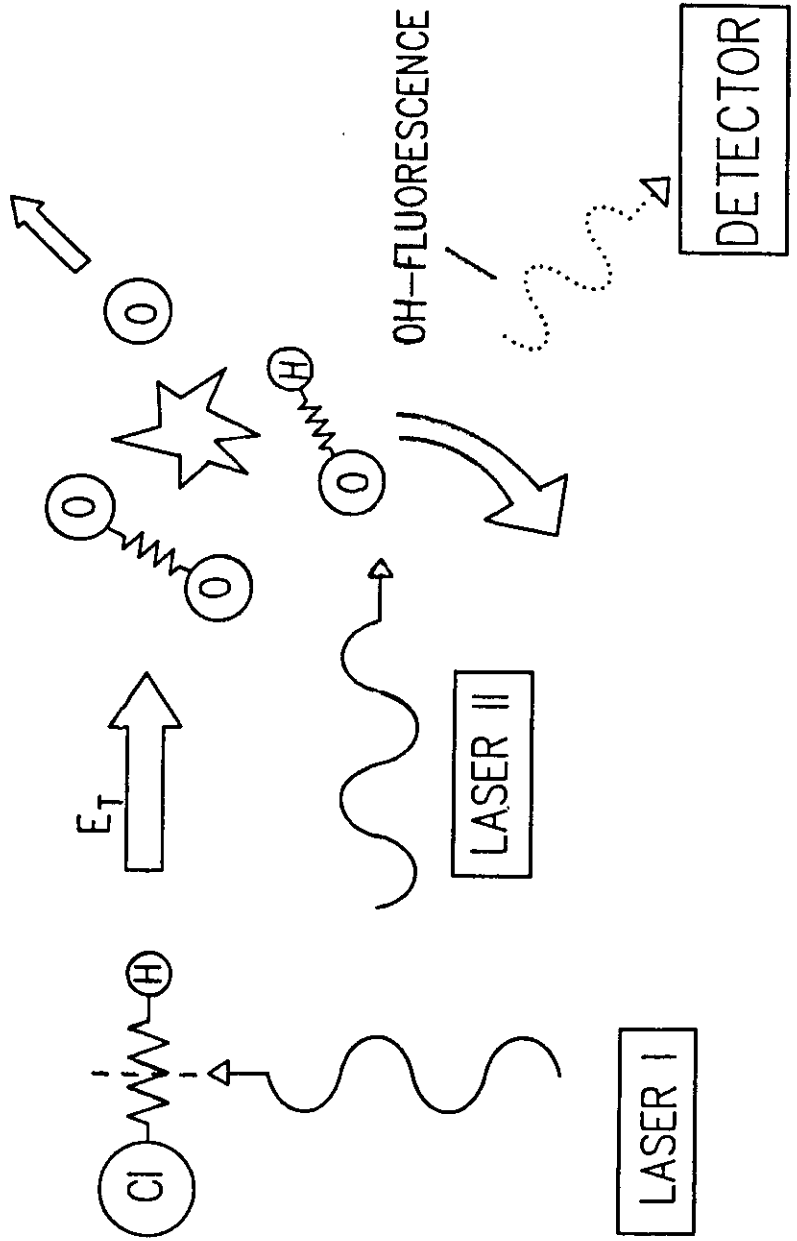
DETECTOR
OH−FLUORESCENCE
O
H
O
O
O
E_T
LASER II
Cl
H
LASER I

Fig 1

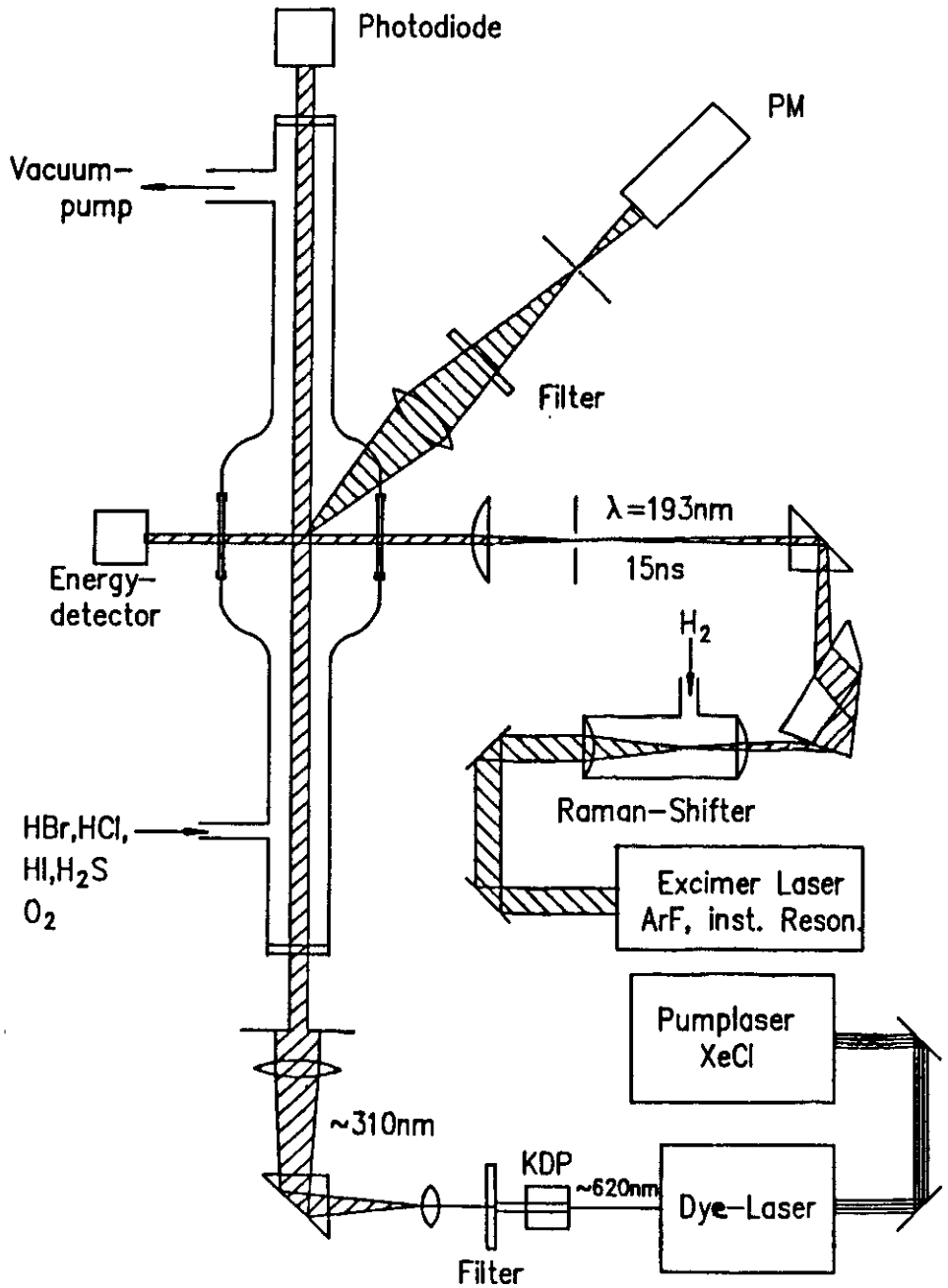
Photodiode
PM
Vacuum–
pump
Filter
λ=193nm
15ns
Energy–
detector
H_2
Raman–Shifter
HBr,HCl,
HI,H_2S
O_2
Excimer Laser
ArF, inst. Reson.
Pumplaser
XeCl
~310nm
KDP
~620nm
Dye–Laser
Filter

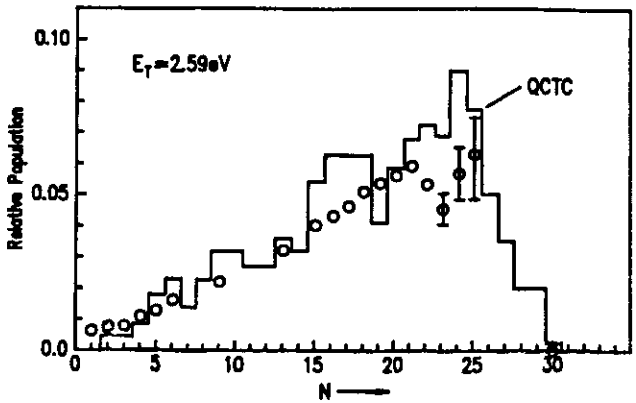
E_T=2.59eV
QCTC
Relative Population
N

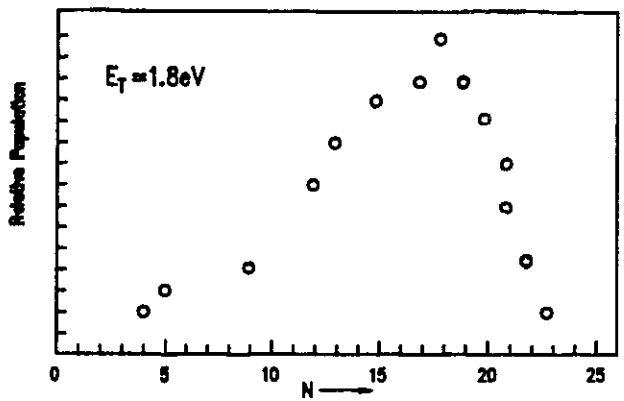
E_T=1.8eV
Relative Population
N

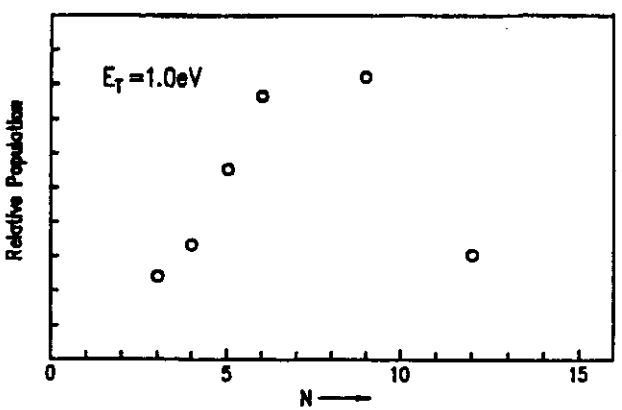
E_T=1.0eV
Relative Population
N

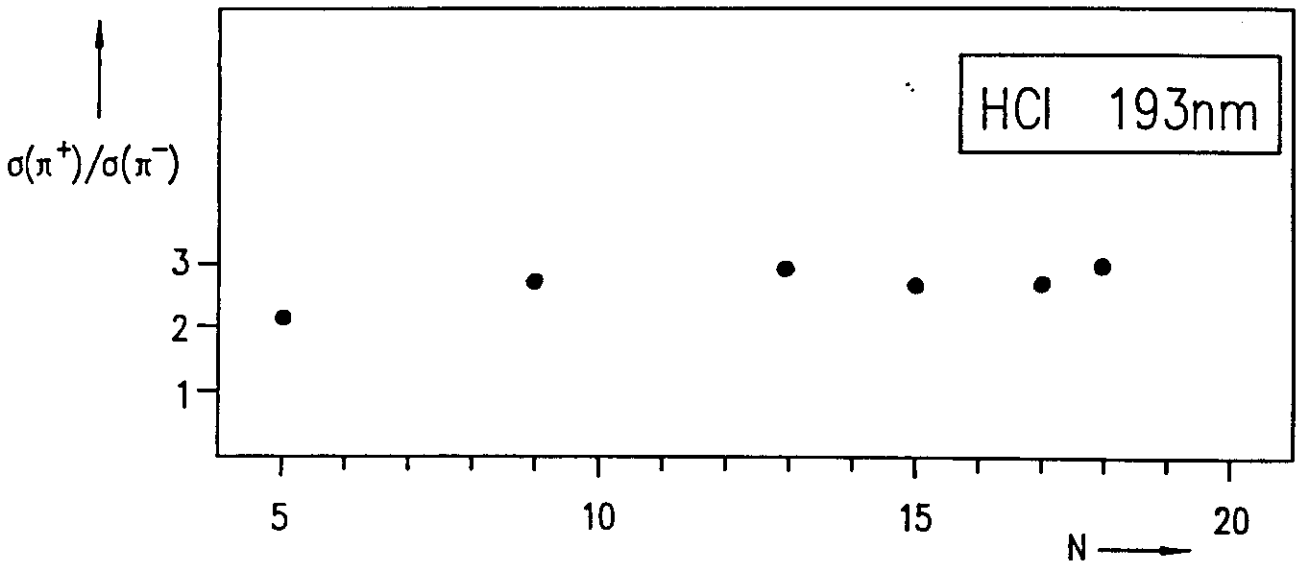

$$H + O_2 \longrightarrow OH + O$$

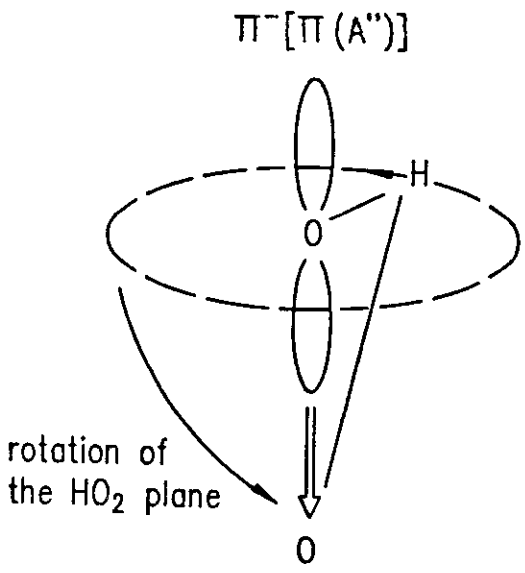

nonplanar reaction pathway

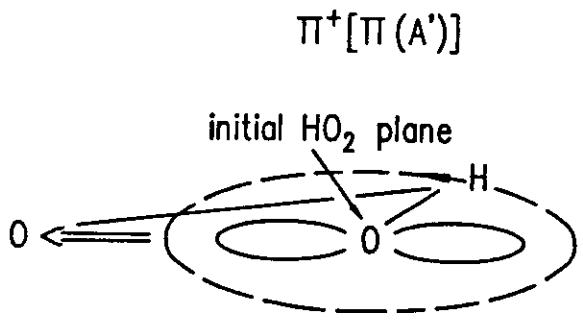

planar reaction pathway

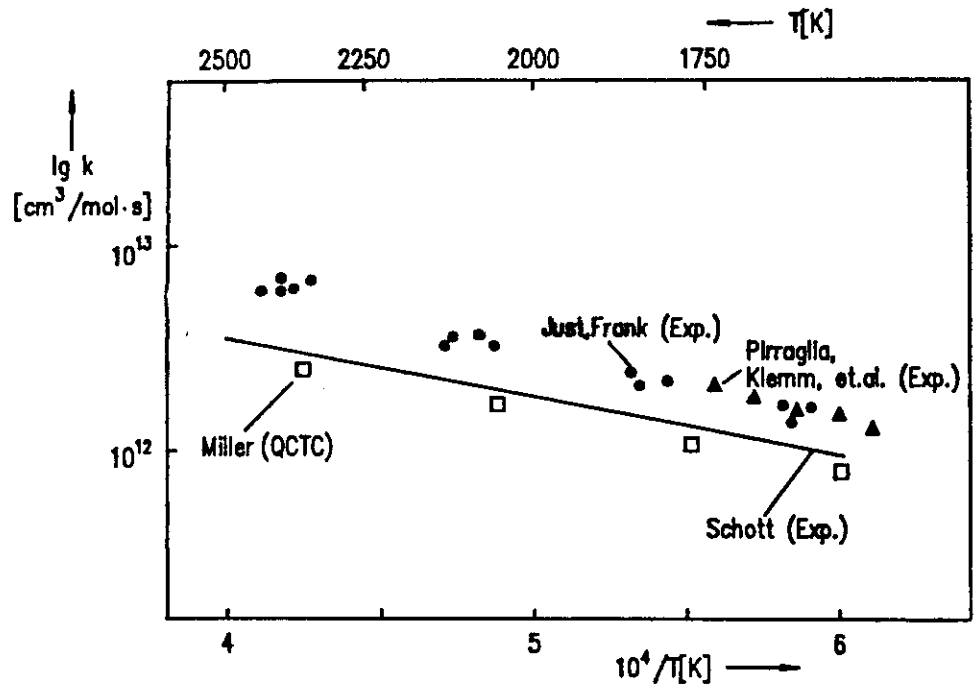
T[K]
2500
2250
2000
1750
lg k
[cm³/mol·s]
10¹³
10¹²
Just,Frank (Exp.)
Pirraglia,
Klemm, et.al. (Exp.)
Miller (QCTC)
Schott (Exp.)
4
5
6
10⁴/T[K]

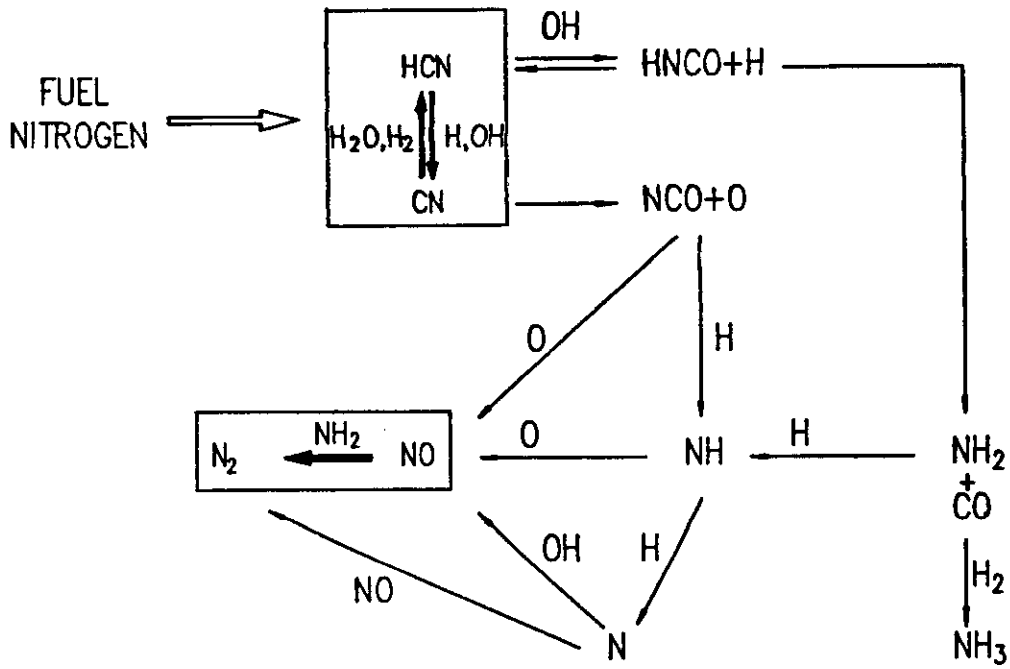
FUEL
NITROGEN
HCN
H₂O,H₂
H,OH
CN
OH
HNCO+H
NCO+O
O
H
N₂
NH₂
NO
O
NH
H
NH₂
+
CO
OH
H
H₂
NO
N
NH₃

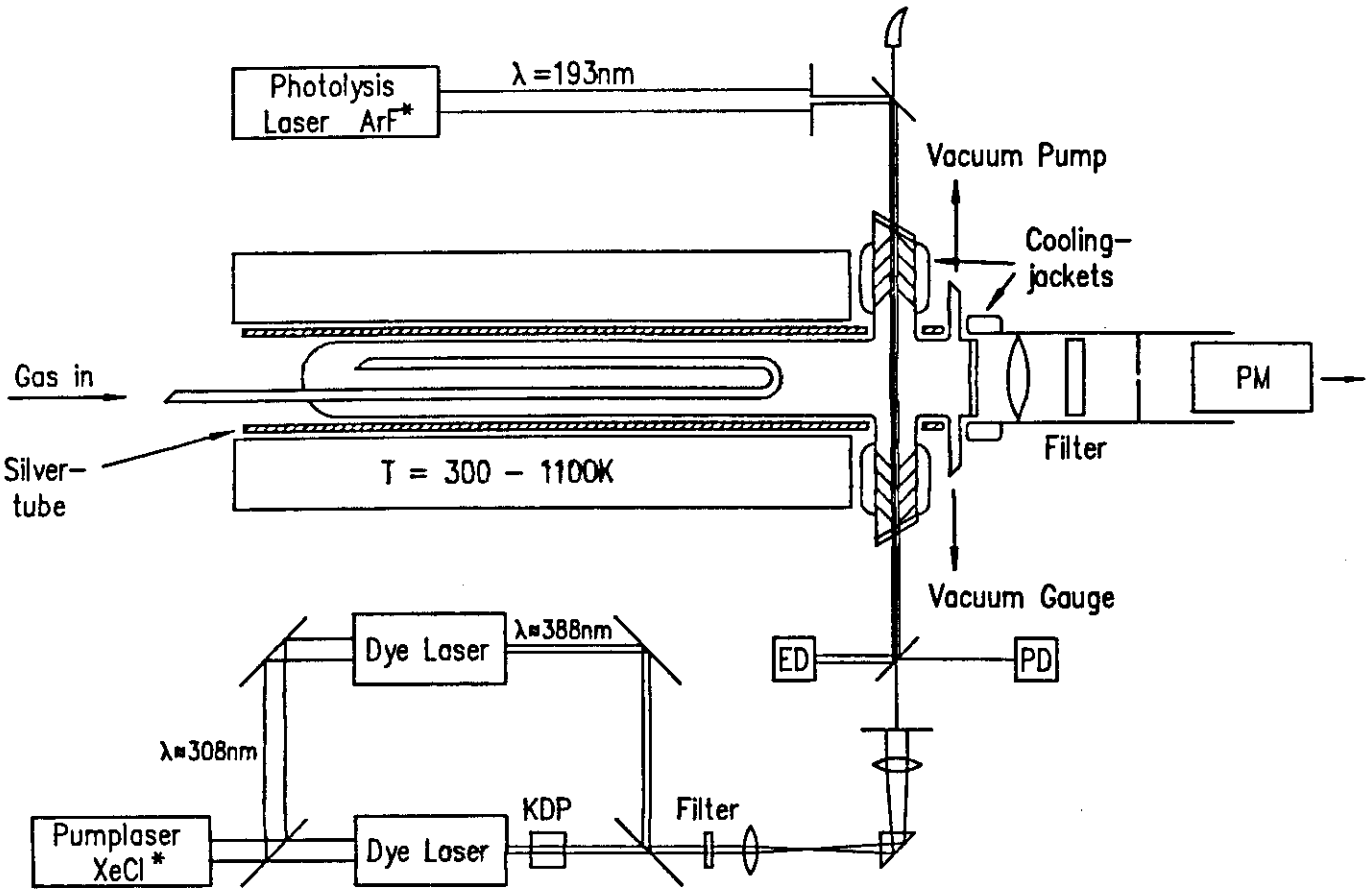
Photolysis Laser ArF*
λ=193nm
Vacuum Pump
Cooling-jackets
Gas in
PM
Filter
Silver-tube
T = 300 – 1100K
Vacuum Gauge
Dye Laser
λ≈388nm
ED
PD
λ≈308nm
KDP
Filter
Pumplaser XeCl*
Dye Laser

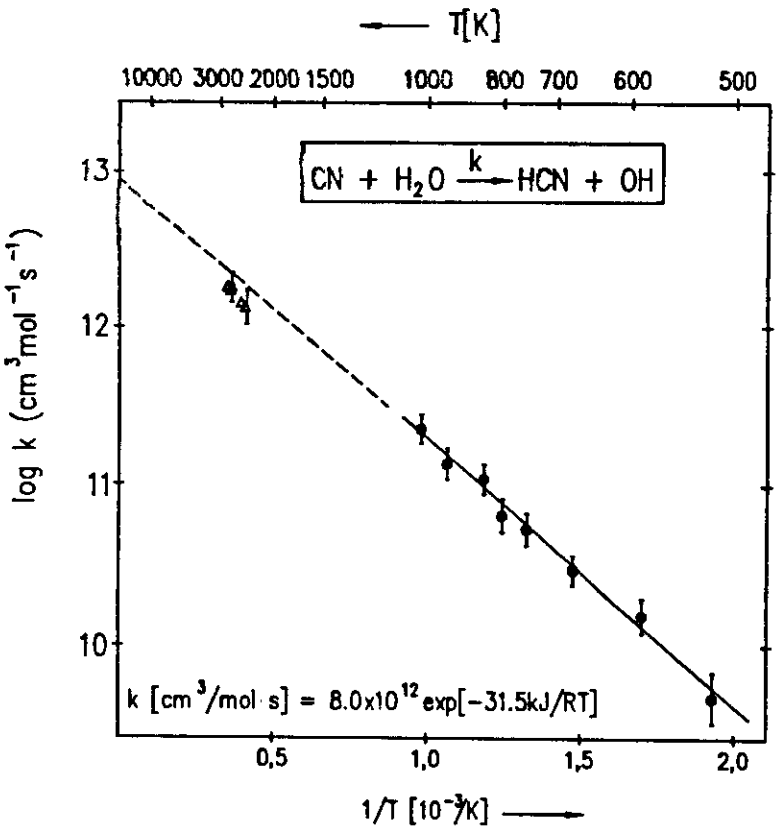
T[K]
10000 3000 2000 1500 1000 800 700 600 500
CN + H2O k HCN + OH
log k (cm3mol-1s-1)
13
12
11
10
k [cm3/mol·s] = 8.0x10^12 exp[-31.5kJ/RT]
0,5
1,0
1,5
2,0
1/T [10-3/K]

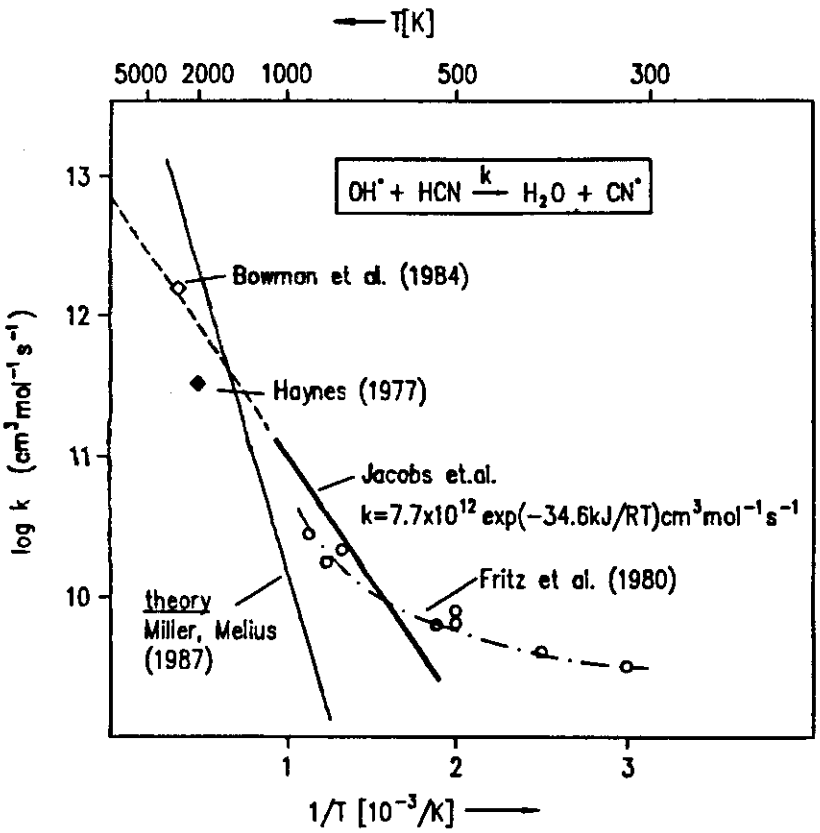
T[K]
5000 2000 1000 500 300
OH* + HCN k H2O + CN*
Bowman et al. (1984)
Haynes (1977)
Jacobs et.al.
k=7.7x10^12 exp(-34.6kJ/RT)cm^3mol^-1s^-1
Fritz et al. (1980)
theory
Miller, Melius
(1987)
log k (cm^3mol^-1s^-1)
13
12
11
10
1
2
3
1/T [10^-3/K]

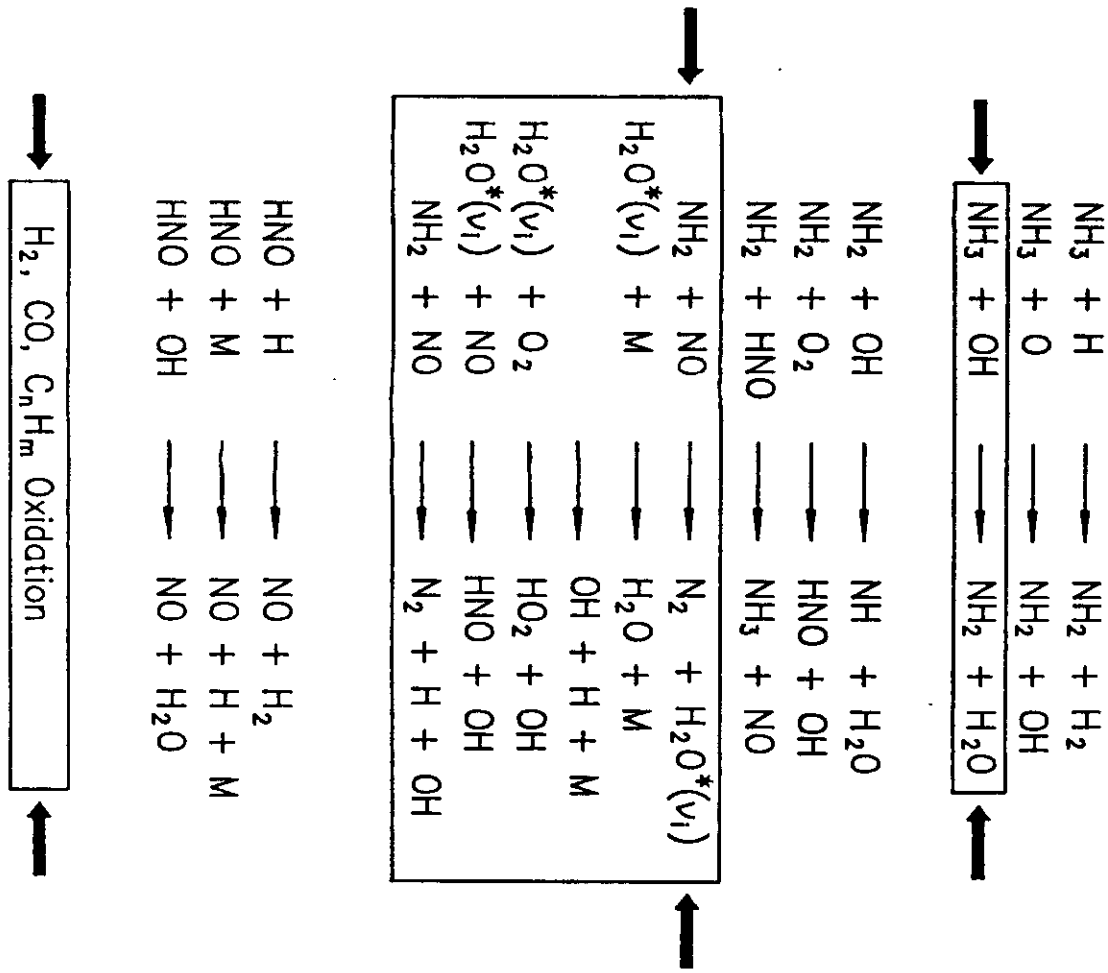
NH3 + H → NH2 + H2
NH3 + O → NH2 + OH
NH3 + OH → NH2 + H2O
NH2 + OH → NH + H2O
NH2 + O2 → HNO + OH
NH2 + HNO → NH3 + NO
NH2 + NO → N2 + H2O*(v1)
H2O*(v1) + M → H2O + M
H2O*(v1) + O2 → HO2 + OH
H2O*(v1) + NO → HNO + OH
NH2 + NO → N2 + H + OH
HNO + H → NO + H2
HNO + M → NO + H + M
HNO + OH → NO + H2O
H2, CO, CnHm Oxidation

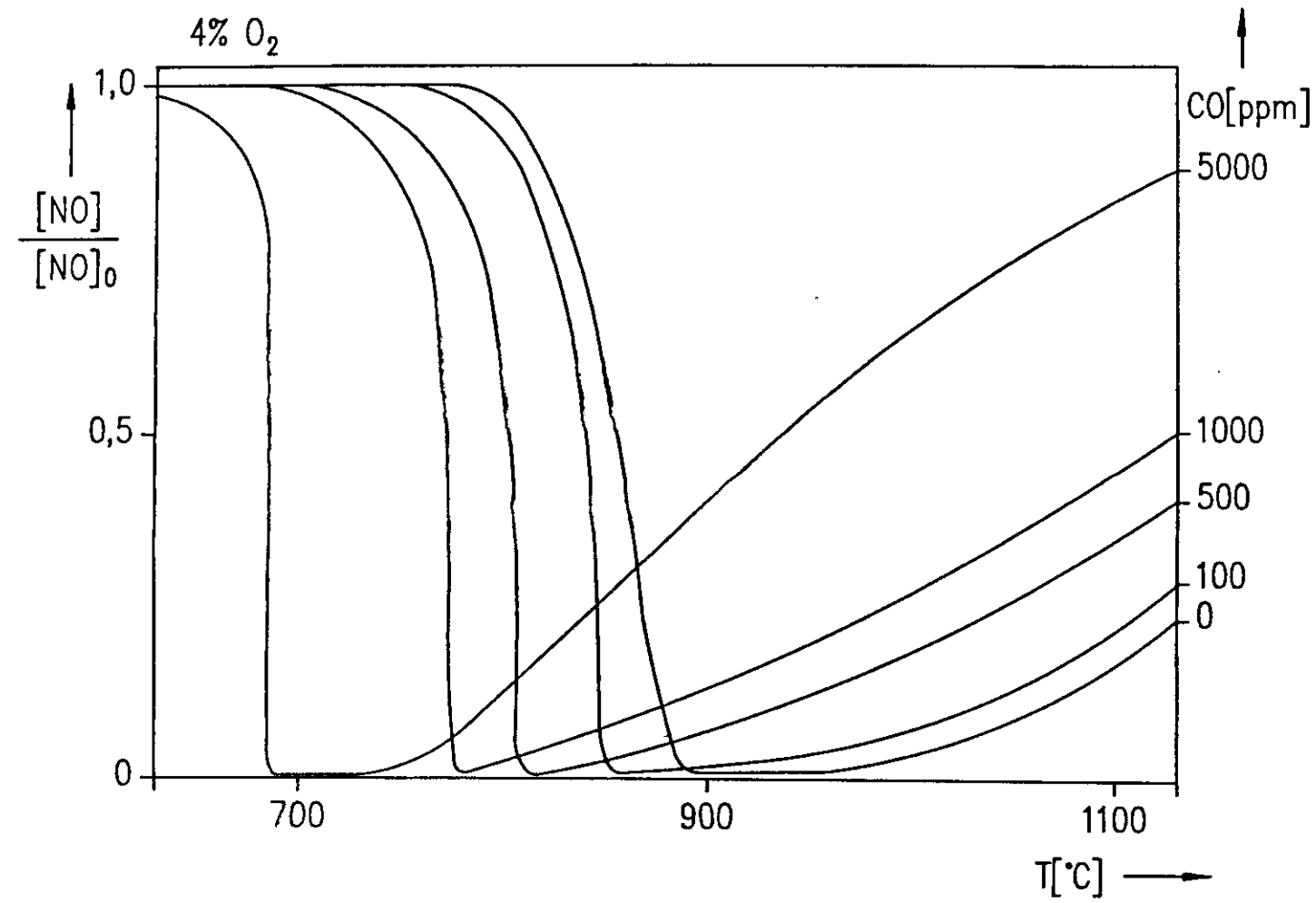
4% O_2
1,0
0,5
0
[NO]/[NO]$_0$
CO[ppm]
5000
1000
500
100
0
700
900
1100
T[°C]

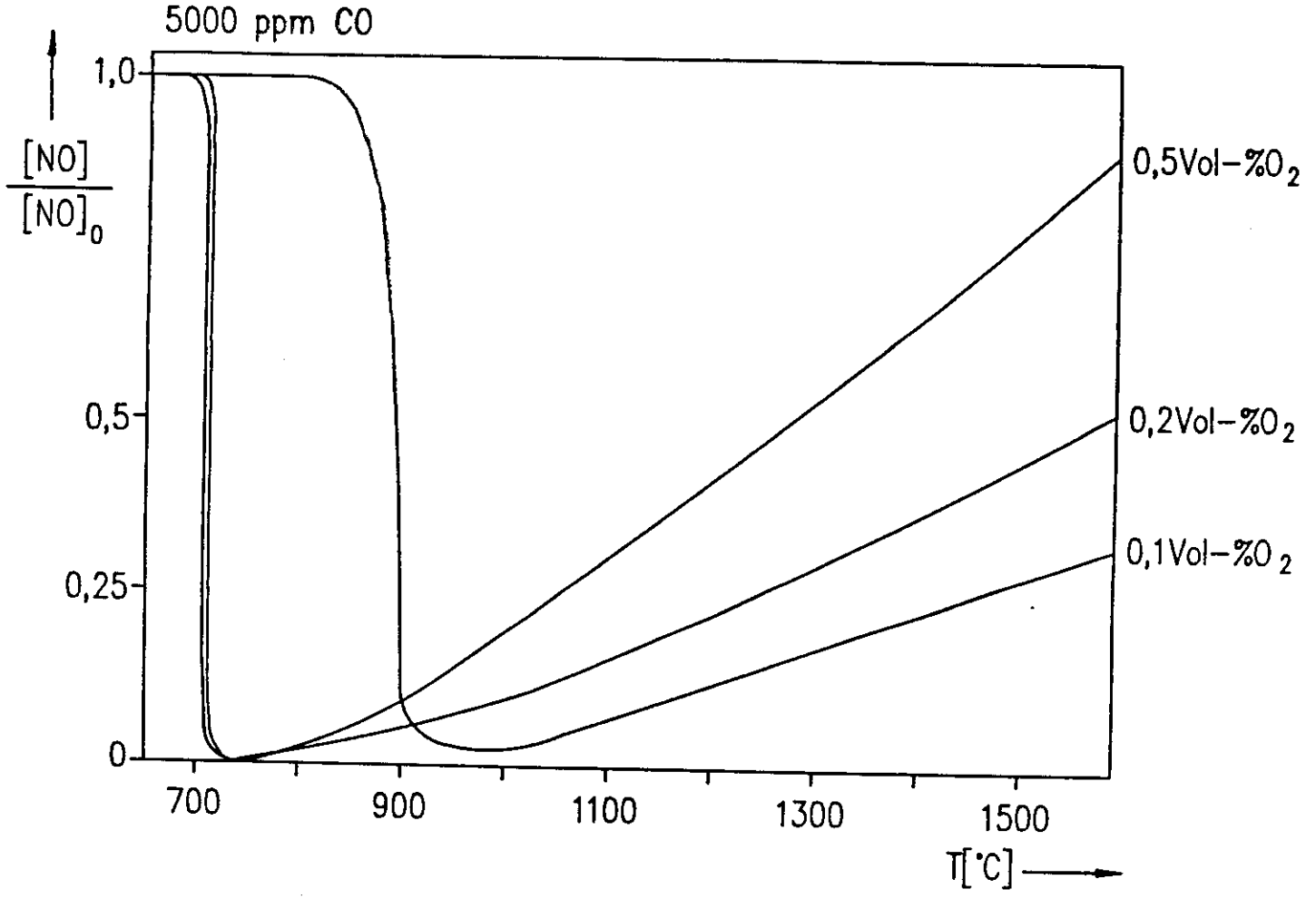
5000 ppm CO
1,0
0,5
0,25
0
[NO]/[NO]$_0$
0,5Vol-%O_2
0,2Vol-%O_2
0,1Vol-%O_2
700
900
1100
1300
1500
T[°C]

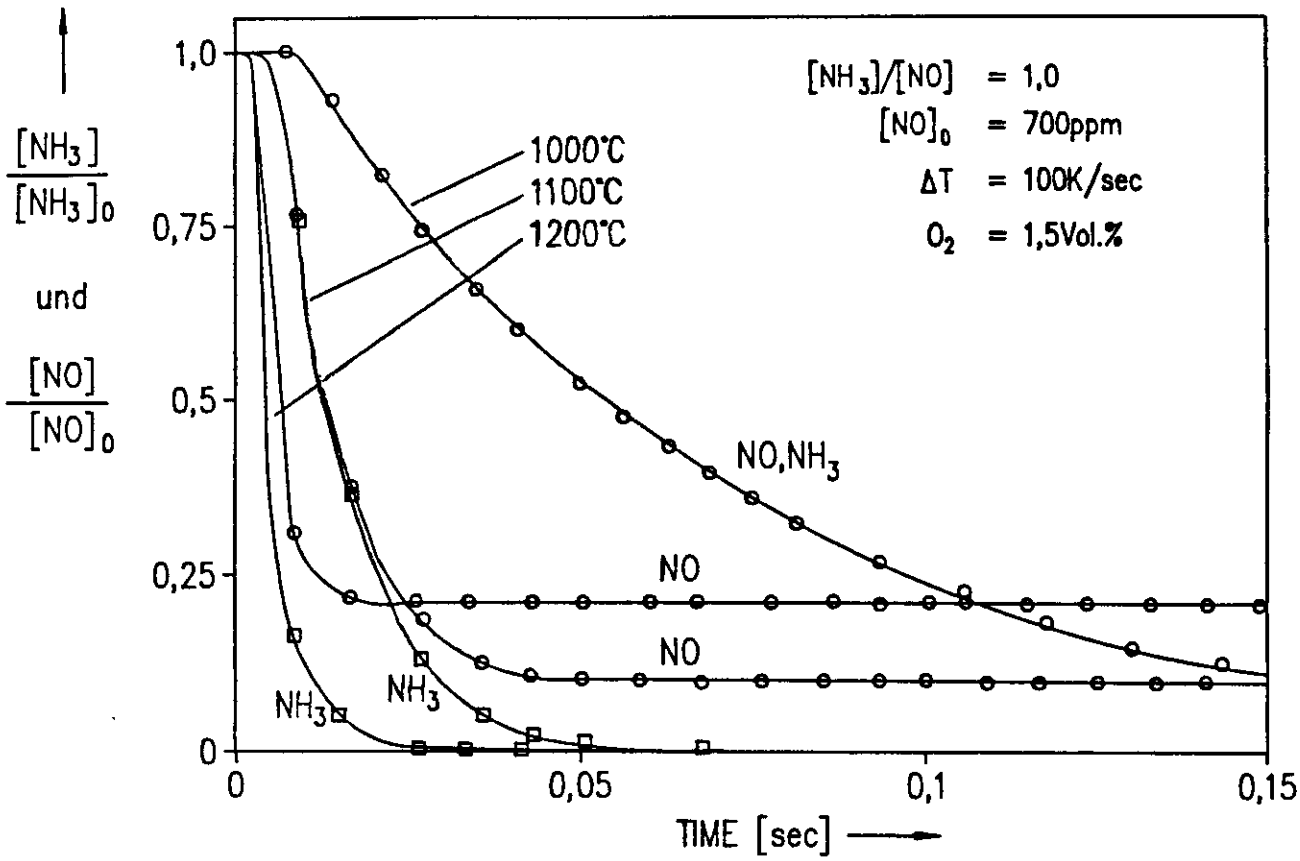
[NH3]/[NO] = 1,0
[NO]0 = 700ppm
ΔT = 100K/sec
O2 = 1,5Vol.%
1000°C
1100°C
1200°C
NO,NH3
NO
NO
NH3
NH3
[NH3] / [NH3]0
und
[NO] / [NO]0
TIME [sec]

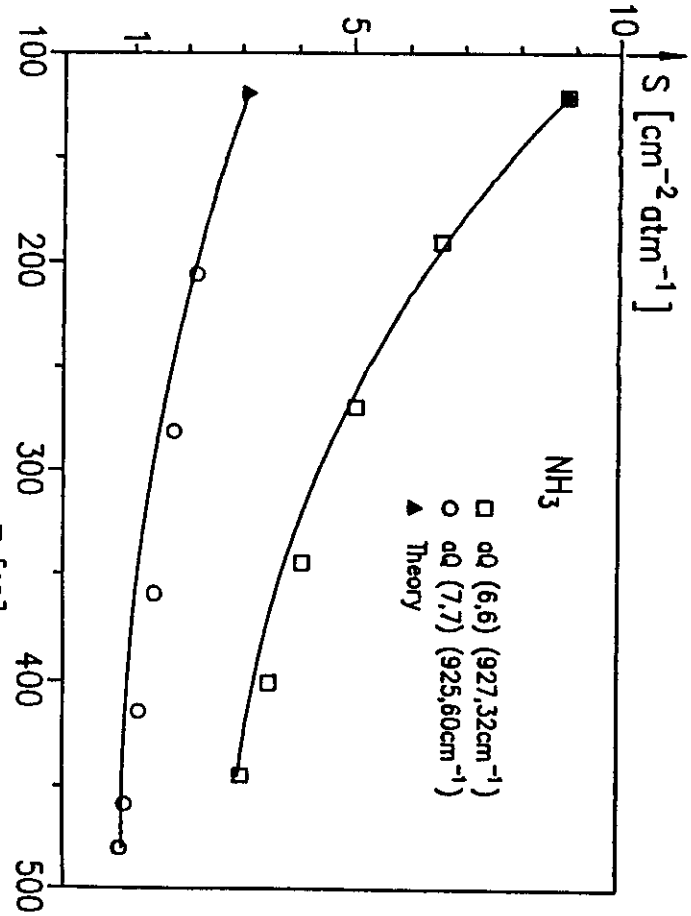
NH3
aQ (6,6) (927,32cm-1)
aQ (7,7) (925,60cm-1)
Theory
S [cm-2atm-1]
T [°C]

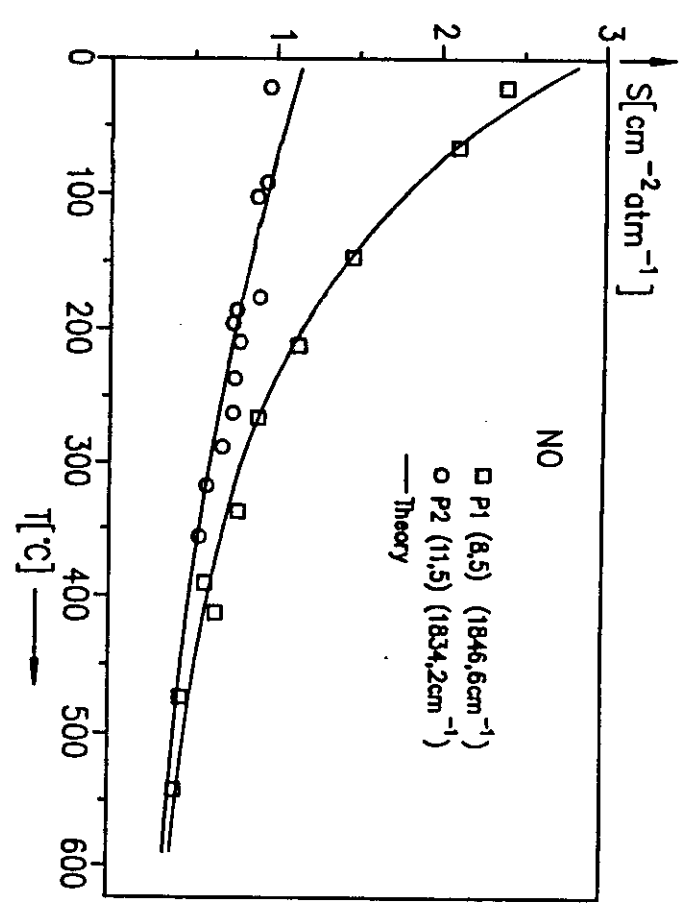
NO
P1 (8,5) (1846,6cm-1)
P2 (11,5) (1834,2cm-1)
Theory
S[cm-2atm-1]
T[°C]

Fig. 12

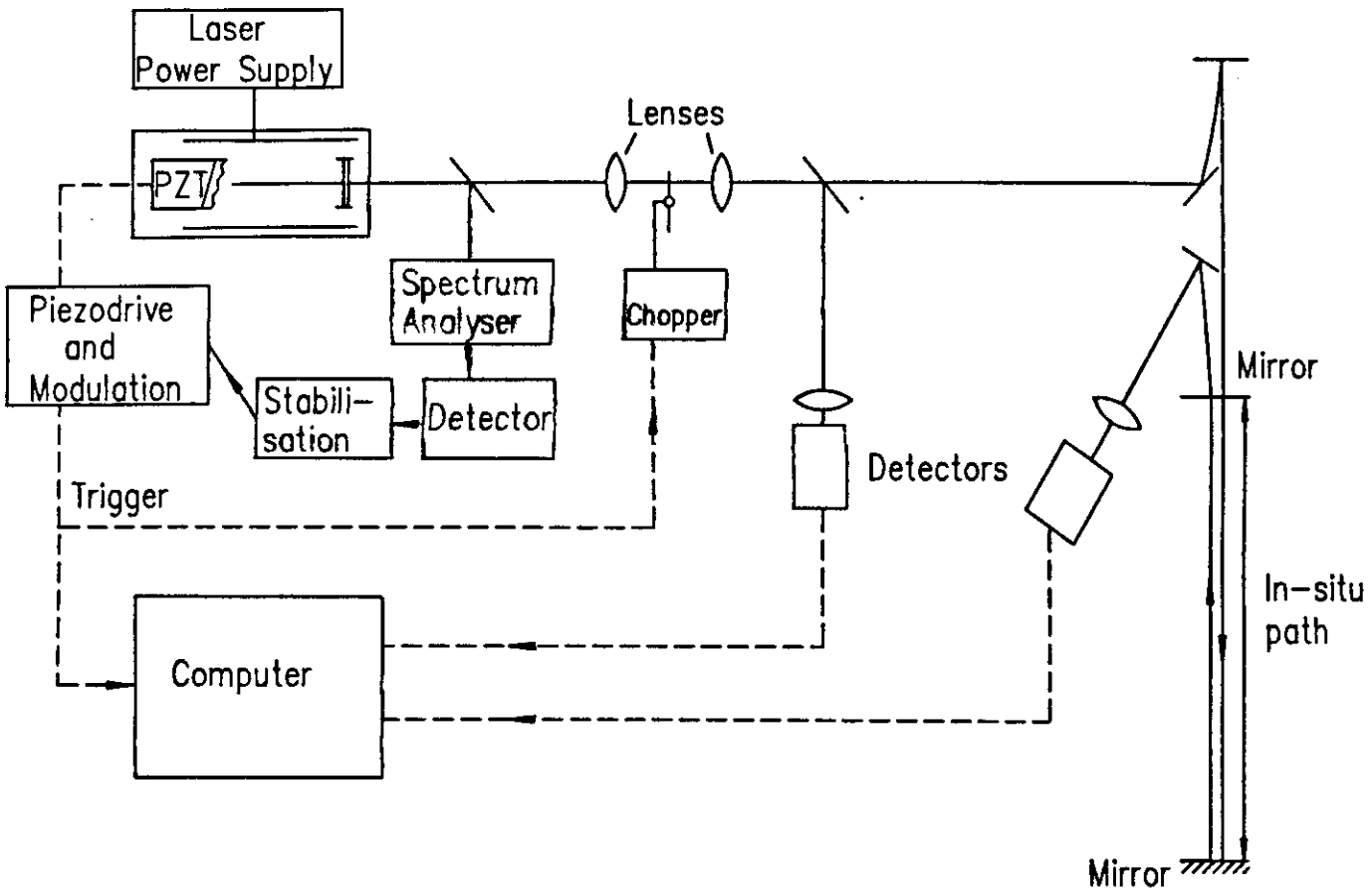
Laser
Power Supply
PZT
Lenses
Spectrum
Analyser
Chopper
Piezodrive
and
Modulation
Stabili-
sation
Detector
Trigger
Detectors
Mirror
In-situ
path
Computer
Mirror

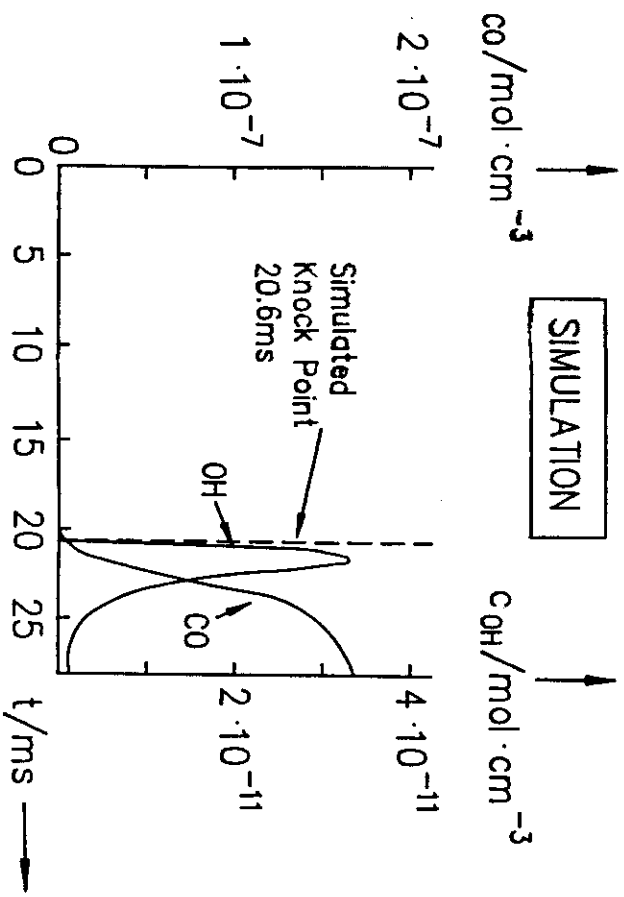
SIMULATION
Simulated
Knock Point
20.6ms
OH
CO
t/ms
c_{OH}/mol·cm^{-3}
co/mol·cm^{-3}

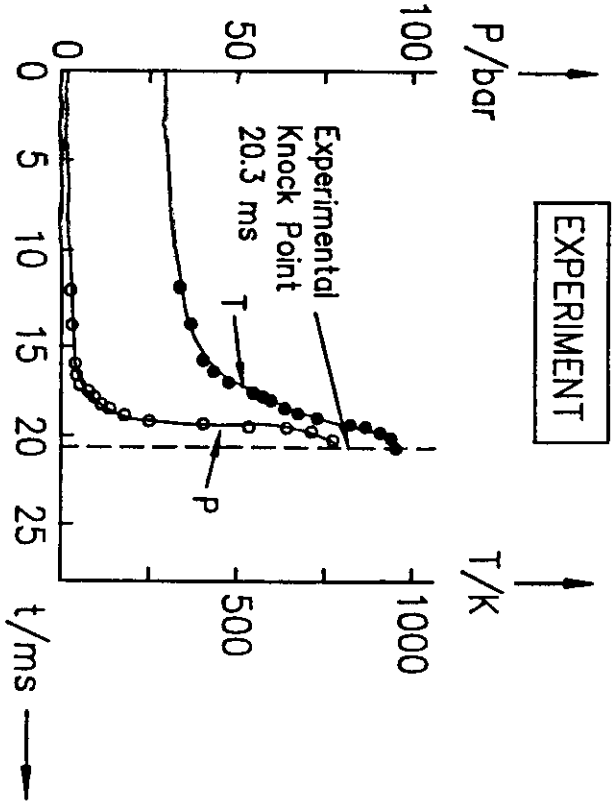
EXPERIMENT
Experimental
Knock Point
20.3 ms
T
P
t/ms
P/bar
T/K

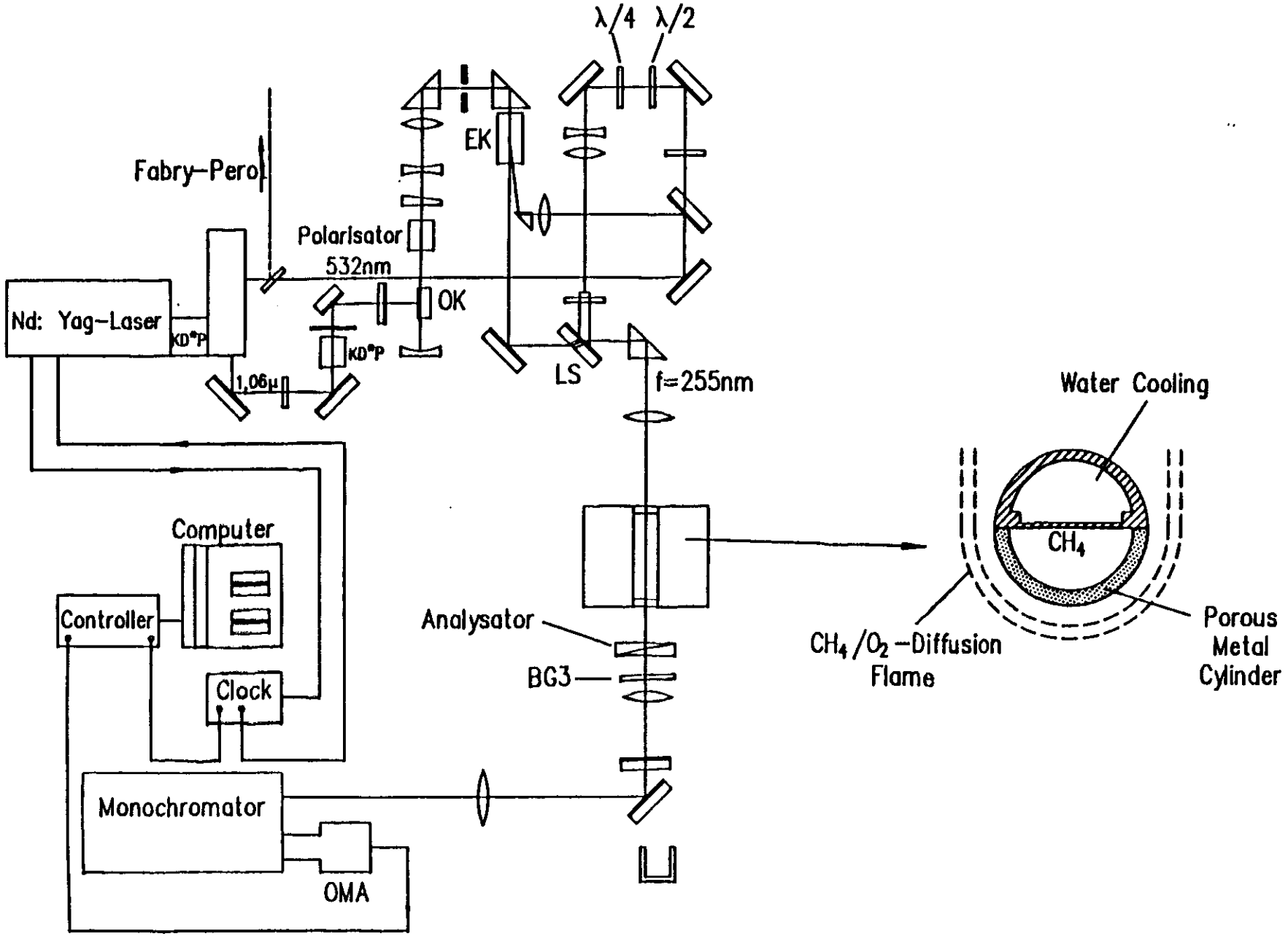
λ/4
λ/2
EK
Fabry–Pero
Polarisator
532nm
OK
Nd: Yag–Laser
KD*P
KD*P
1,06µ
LS
f=255nm
Water Cooling
CH4
Computer
Controller
Clock
Analysator
BG3
CH4 /O2 –Diffusion
Flame
Porous
Metal
Cylinder
Monochromator
OMA

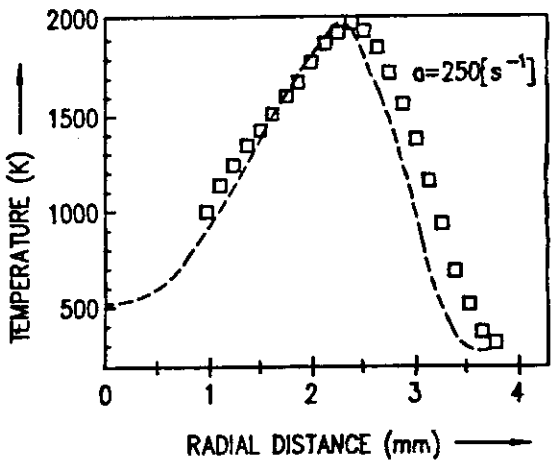
TEMPERATURE (K)
2000
1500
1000
500
0
1
2
3
4
RADIAL DISTANCE (mm)
a=250[s⁻¹]

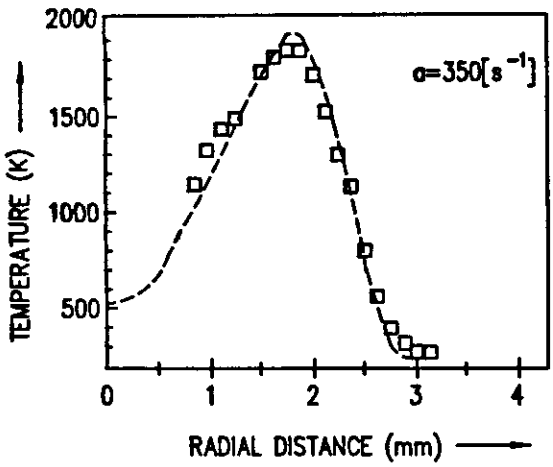
TEMPERATURE (K)
2000
1500
1000
500
0
1
2
3
4
RADIAL DISTANCE (mm)
a=350[s⁻¹]

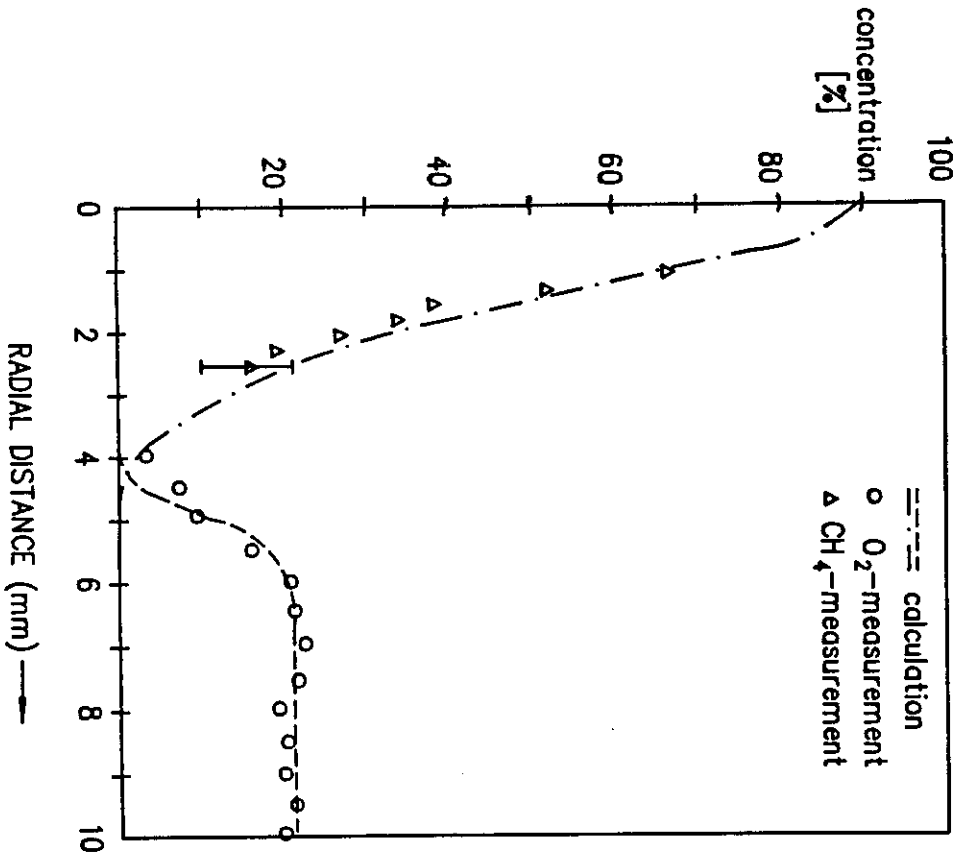
RADIAL DISTANCE (mm)
0
2
4
6
8
10
20
40
60
80
100
concentration [%]
calculation
o O2-measurement
Δ CH4-measurement

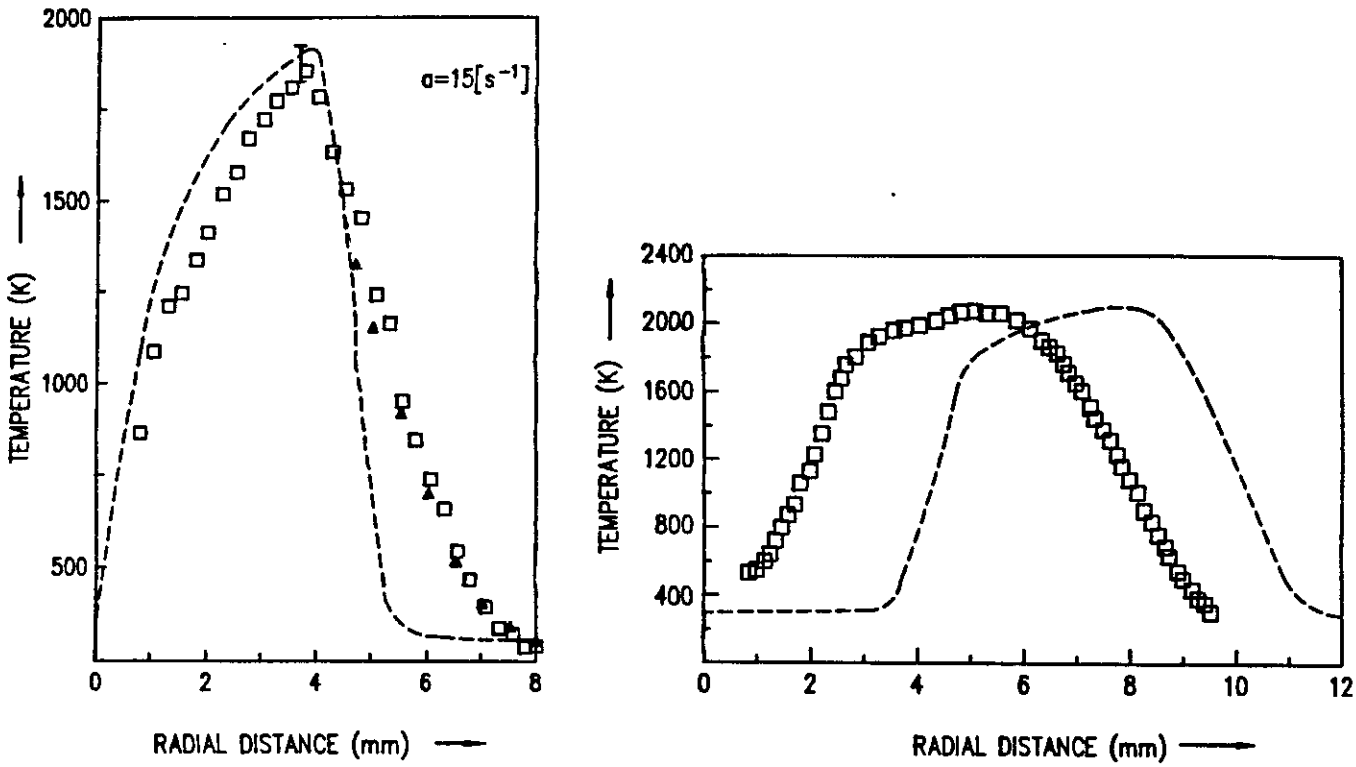
2000
1500
1000
500
TEMPERATURE (K)
a=15[s⁻¹]
0
2
4
6
8
RADIAL DISTANCE (mm)
2400
2000
1600
1200
800
400
TEMPERATURE (K)
0
2
4
6
8
10
12
RADIAL DISTANCE (mm)

Fig. 18

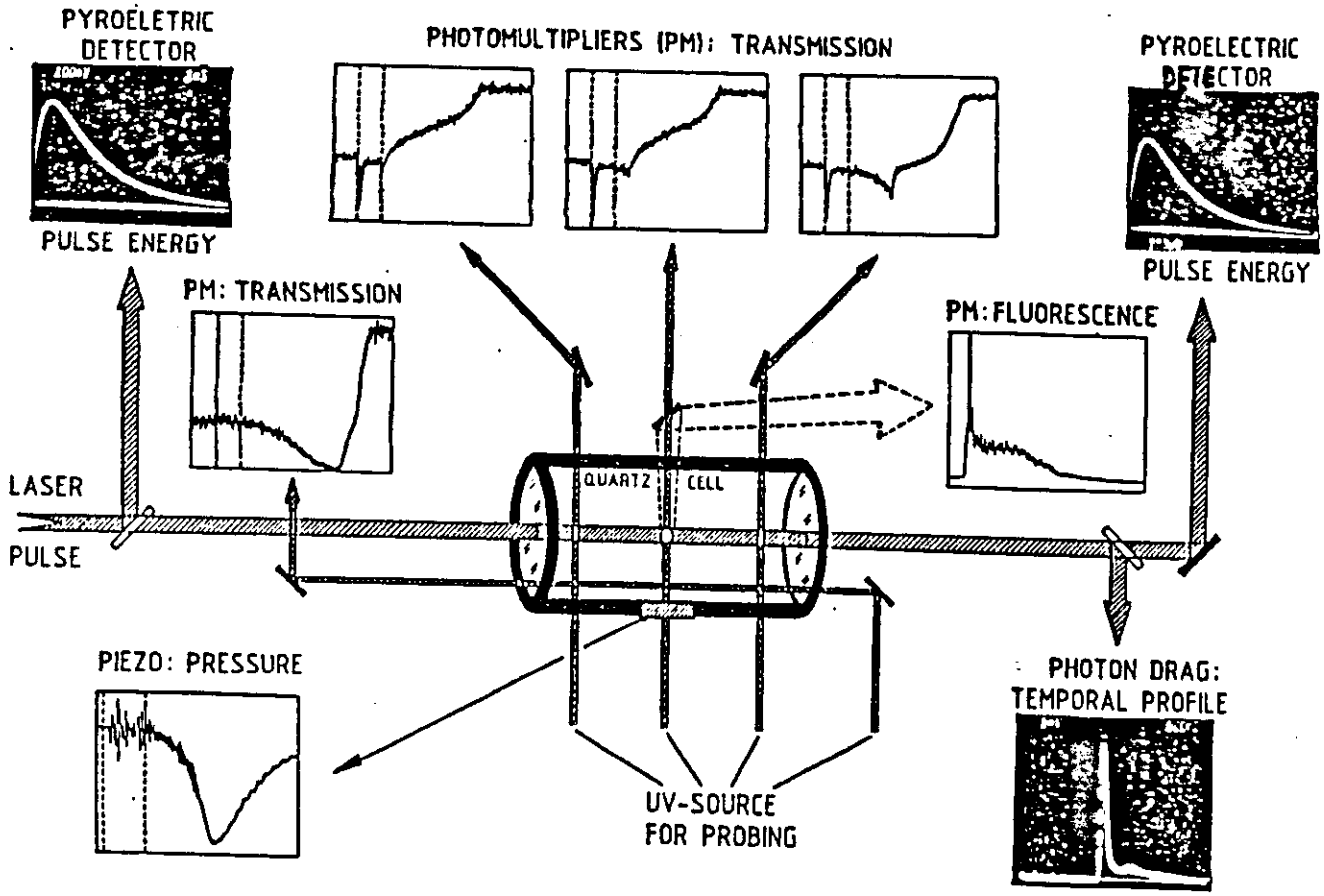
PYROELETRIC DETECTOR
PULSE ENERGY
PHOTOMULTIPLIERS (PM): TRANSMISSION
PYROELECTRIC DETECTOR
PULSE ENERGY
PM: TRANSMISSION
PM: FLUORESCENCE
LASER PULSE
QUARTZ CELL
PIEZO: PRESSURE
PHOTON DRAG: TEMPORAL PROFILE
UV-SOURCE FOR PROBING

Fig. 19

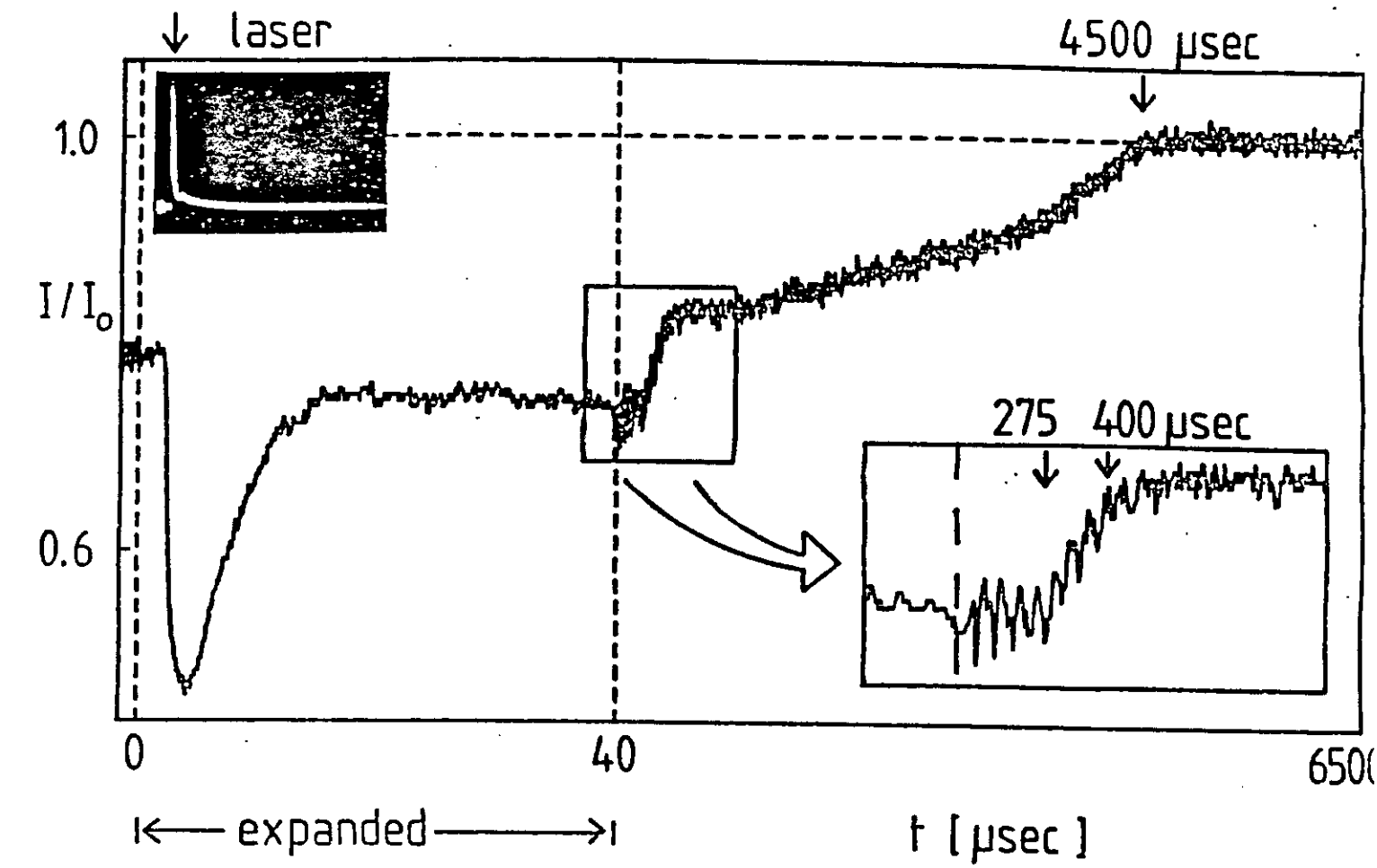
laser
4500 µsec
1.0
I / I$_o$
0.6
275 400 µsec
0
40
650(
expanded
t [µsec]

Fig. 20

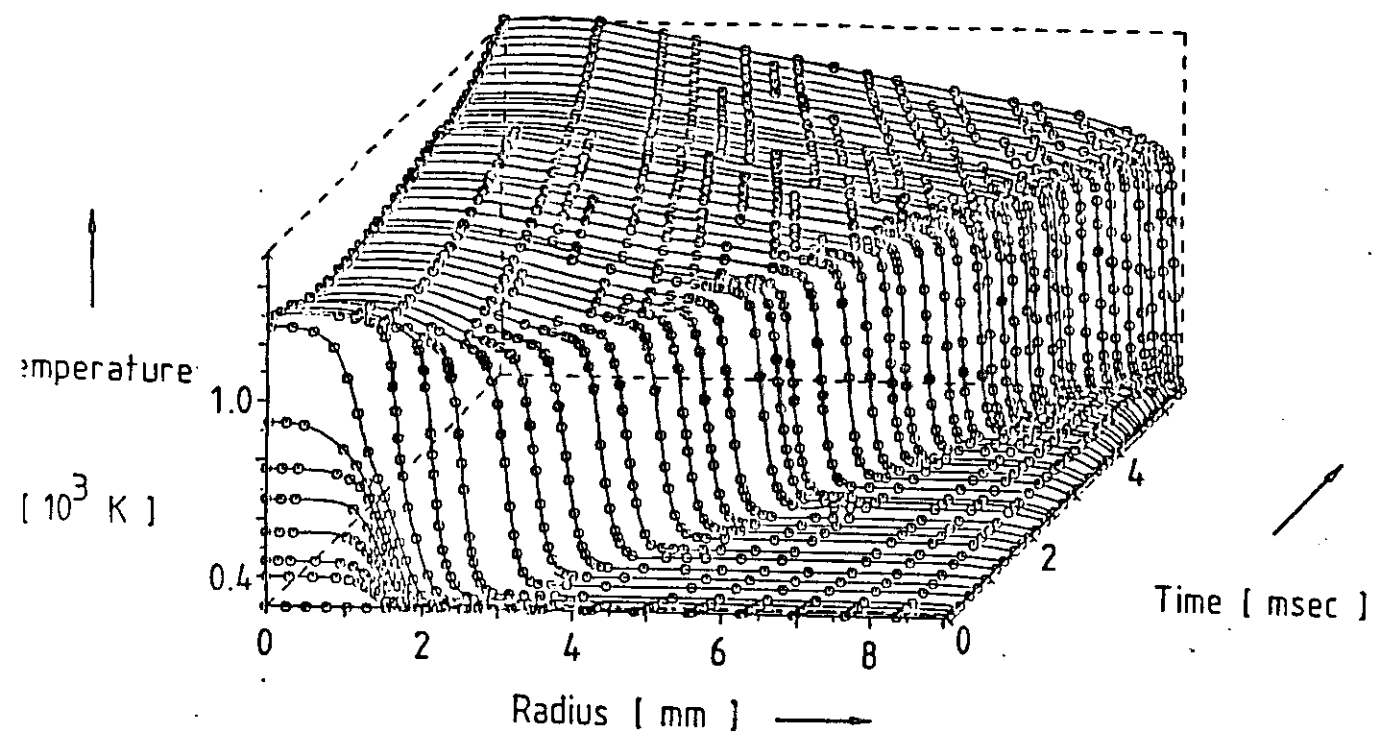
emperature
[10^3 K]
1.0
0.4
0
2
4
6
8
0
2
4
Time [msec]
Radius [mm]

Fig. 21

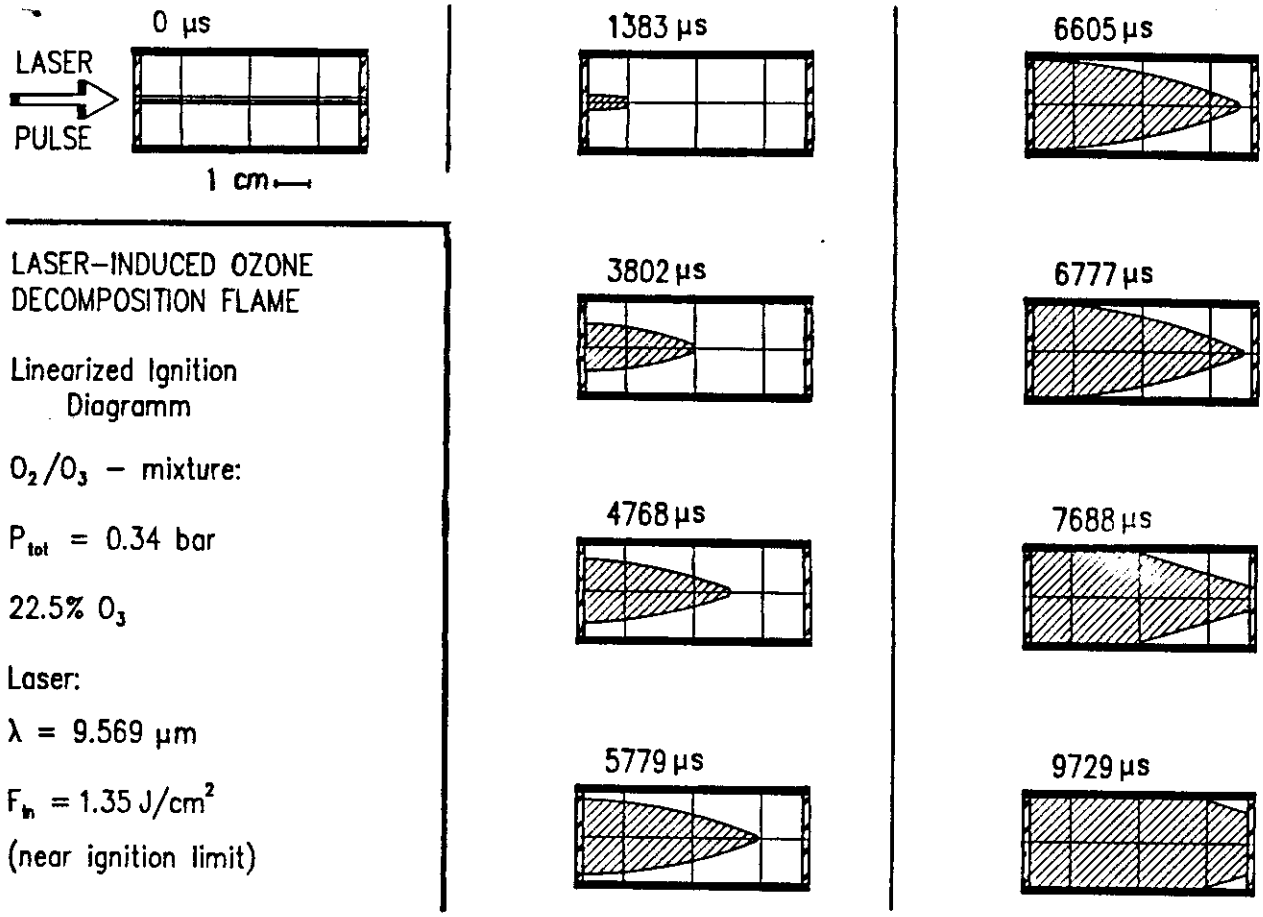

LASER–INDUCED OZONE DECOMPOSITION FLAME

Linearized Ignition Diagramm

O_2/O_3 – mixture:

P_{tot} = 0.34 bar

22.5% O_3

Laser:

λ = 9.569 µm

F_{th} = 1.35 J/cm²

(near ignition limit)

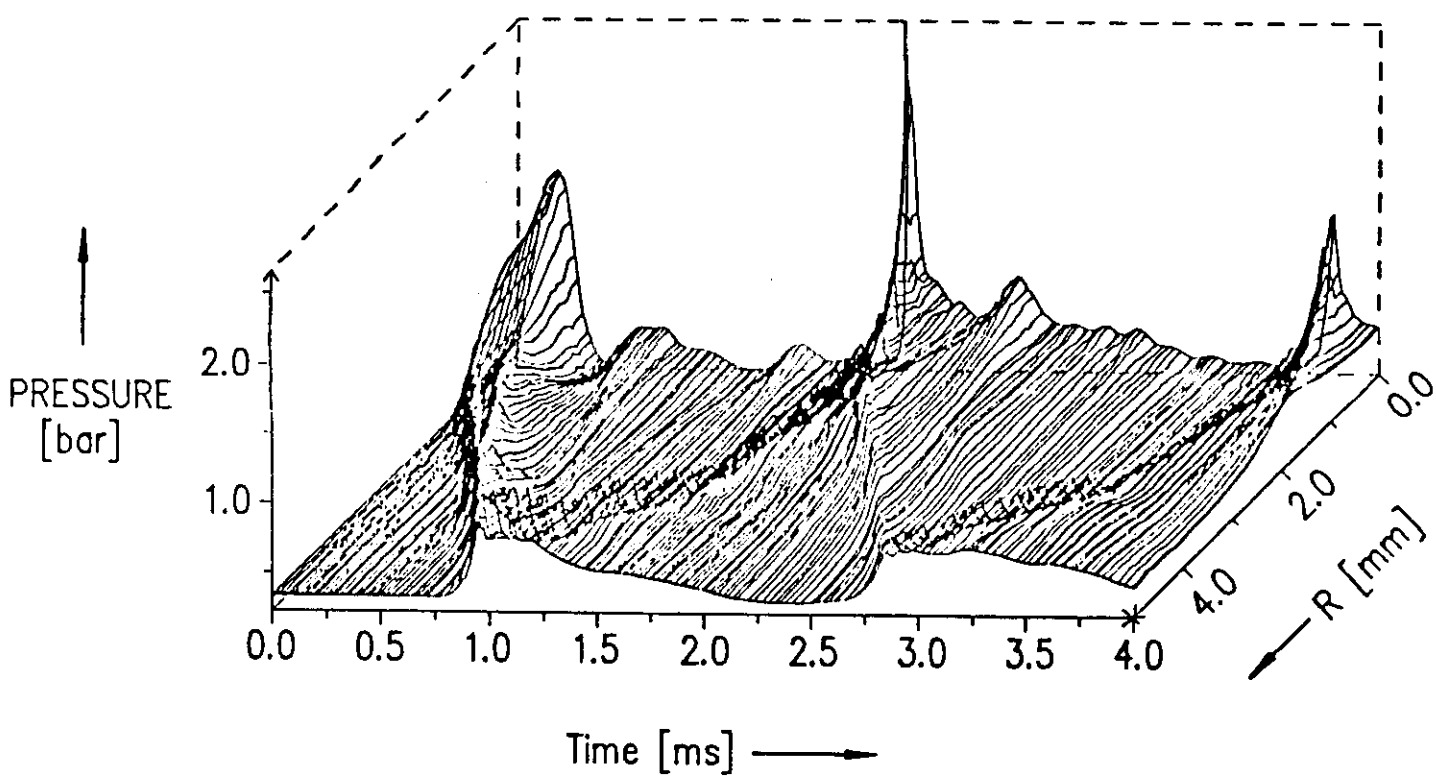

Fig. 23a

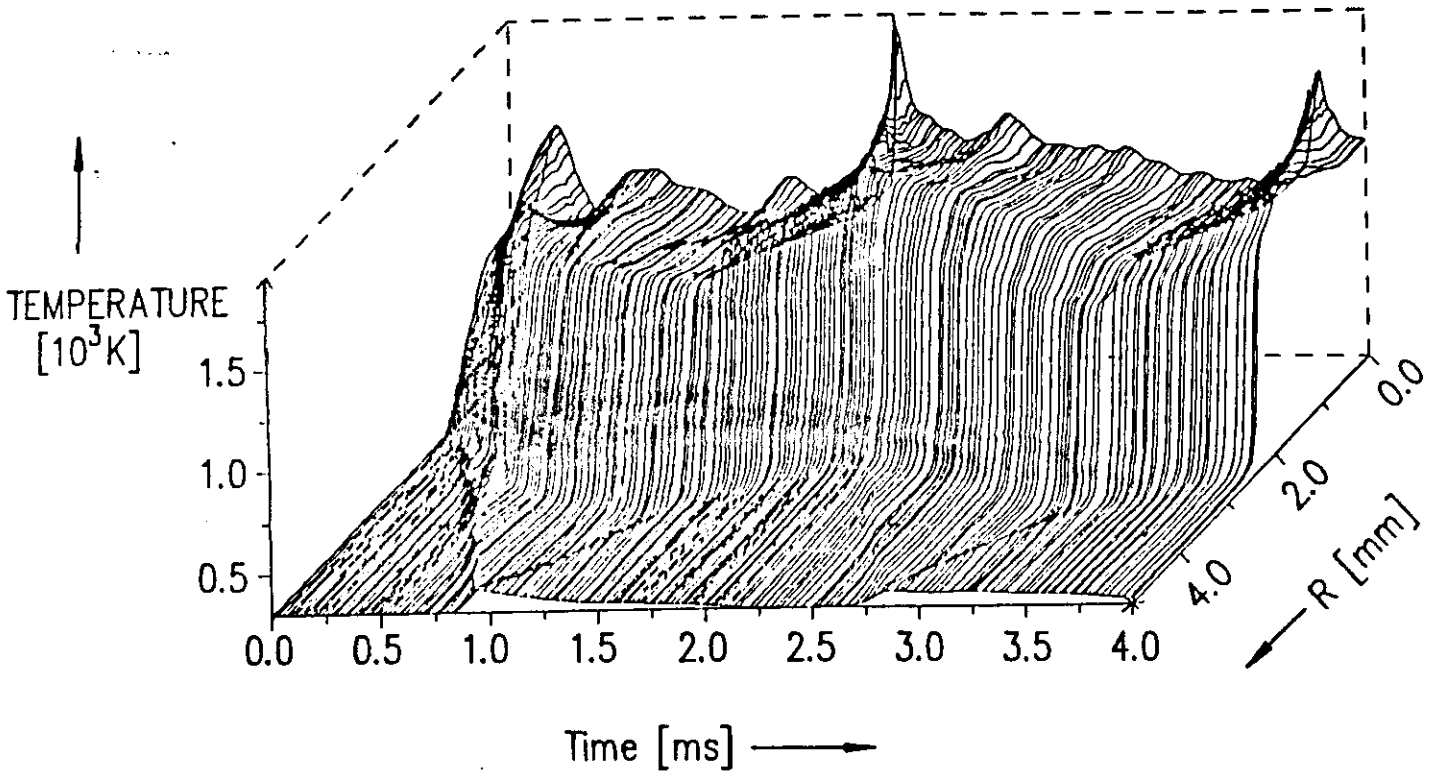

Fig. 23b

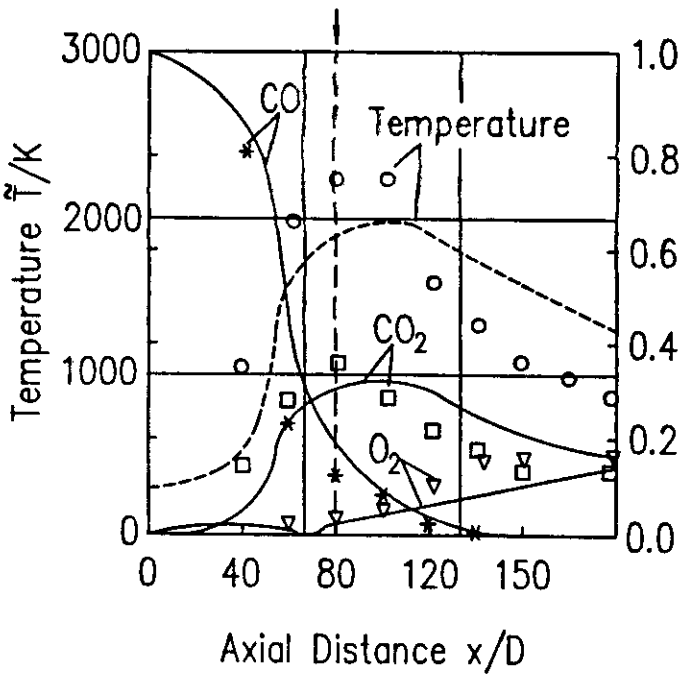

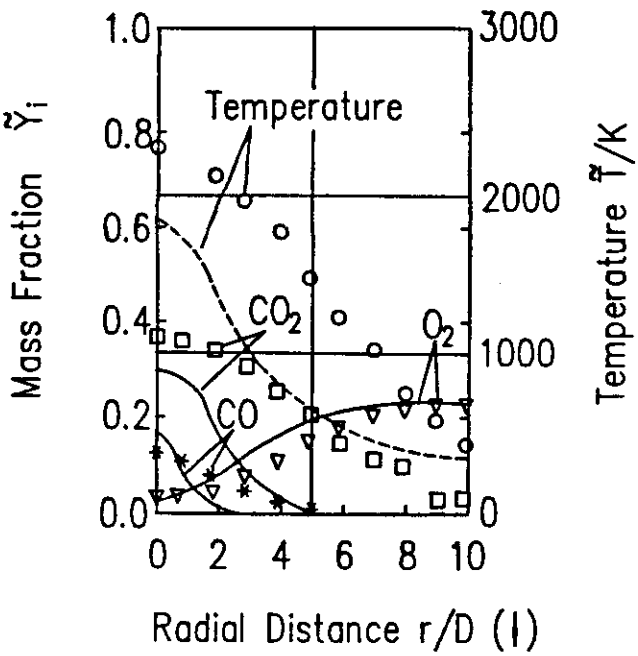

Fig. 24

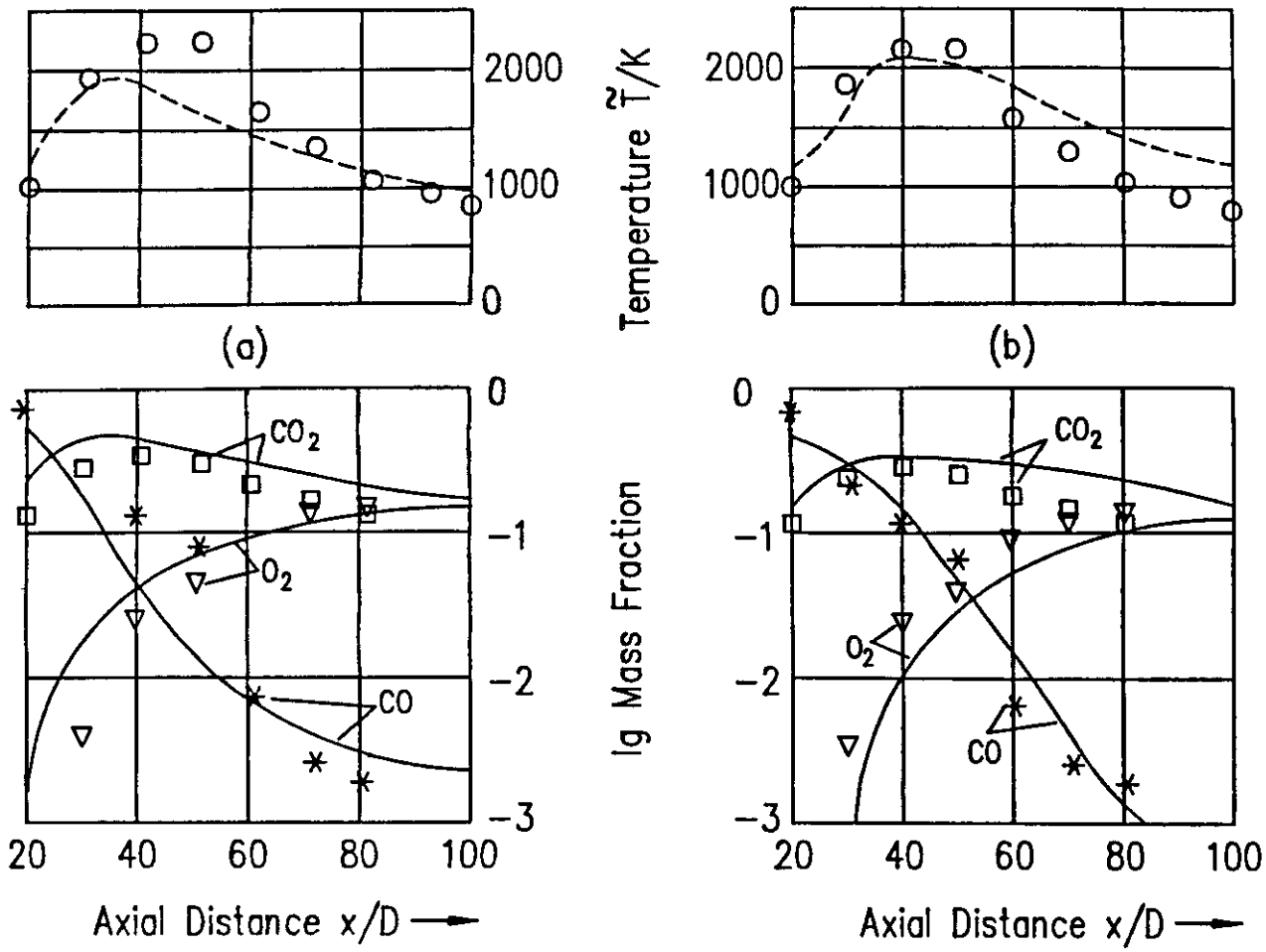
2000
1000
0
(a)
(b)
Temperature $\tilde{T}$/K
CO_2
O_2
CO
0
−1
−2
−3
lg Mass Fraction
20
40
60
80
100
Axial Distance x/D

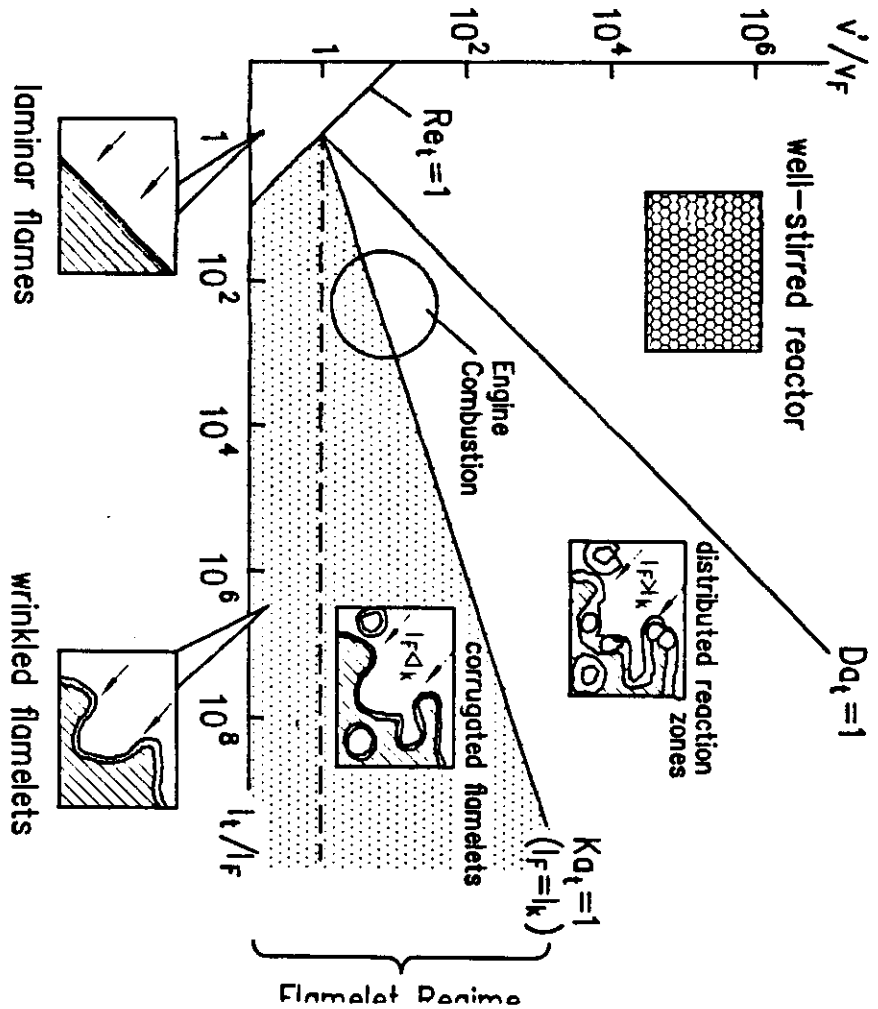
v'/v_F
10^2
10^4
10^6
$Re_t=1$
well-stirred reactor
laminar flames
wrinkled flamelets
Engine Combustion
distributed reaction zones
corrugated flamelets
$Da_t=1$
$Ka_t=1$
$(l_F=l_k)$
l_t/l_F
10^8
Flamelet Regime

Fig. 26

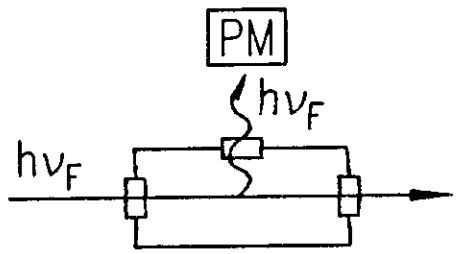

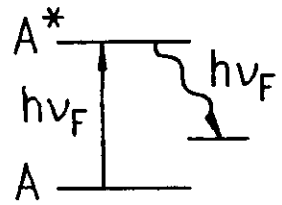

Particle number — Einstein–Coefficients

$$I_{LIF} \sim I_{Laser} \cdot V \cdot N_s \cdot B \cdot F_{vj}(T)\,[A/(A+Q)]$$

Volume — Distribution — Quenching

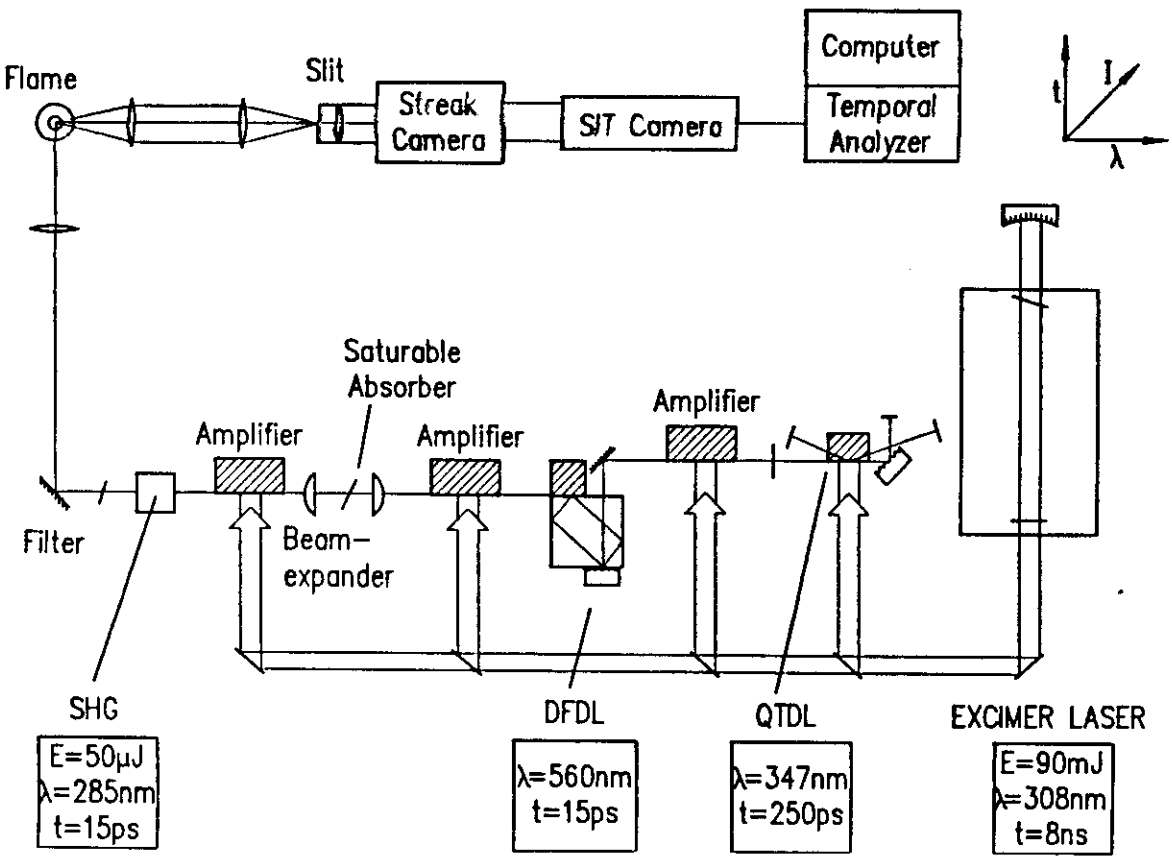

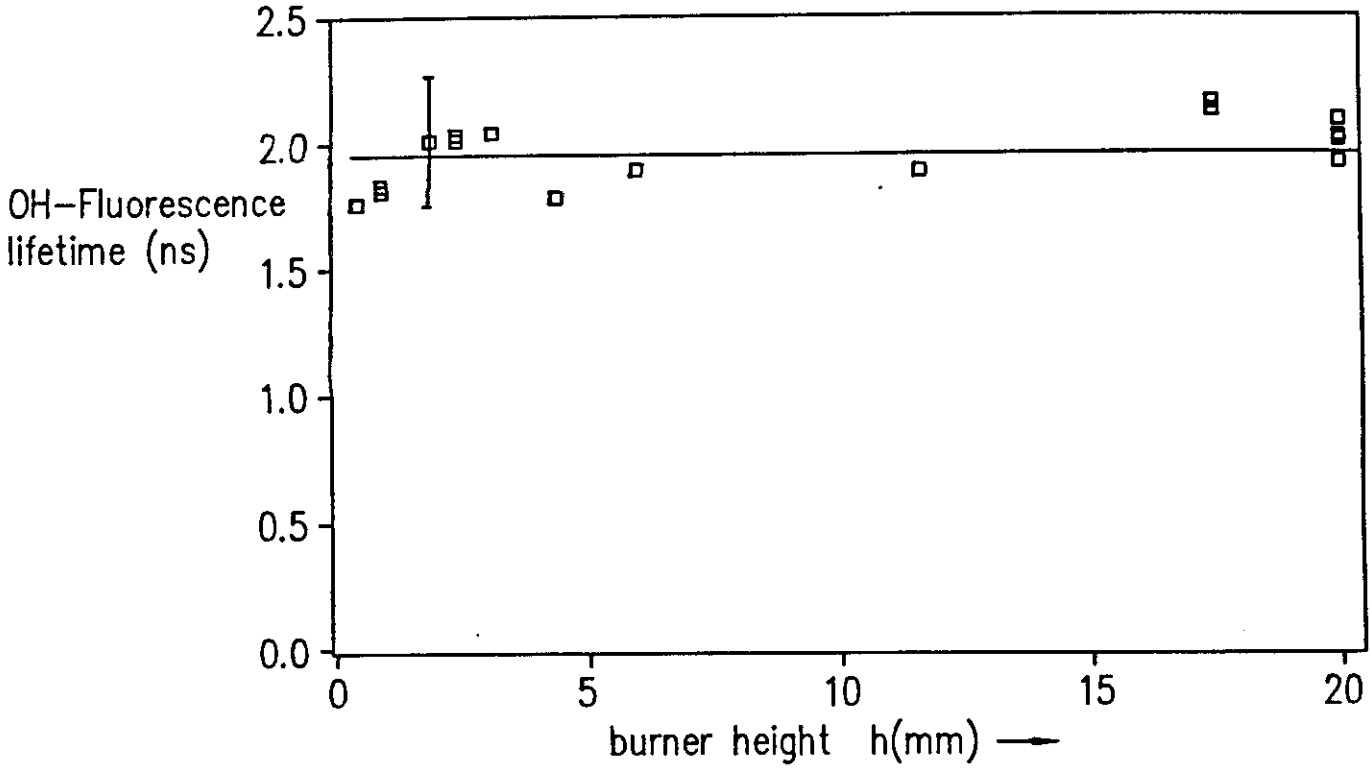
2.5
2.0
1.5
1.0
0.5
0.0
OH–Fluorescence
lifetime (ns)
0
5
10
15
20
burner height h(mm) —

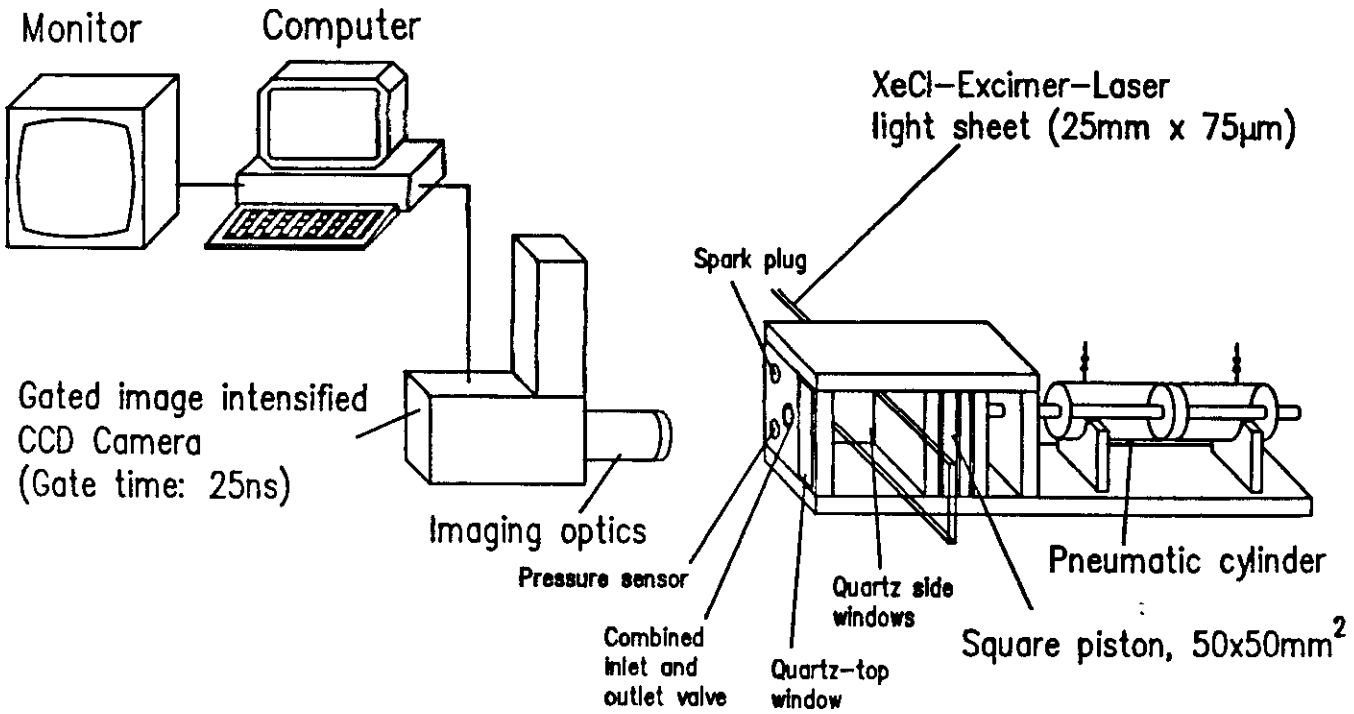
Monitor
Computer
XeCl–Excimer–Laser
light sheet (25mm x 75µm)
Spark plug
Gated image intensified
CCD Camera
(Gate time: 25ns)
Imaging optics
Pressure sensor
Combined
inlet and
outlet valve
Quartz-top
window
Quartz side
windows
Pneumatic cylinder
Square piston, 50x50mm²

Fig. 30

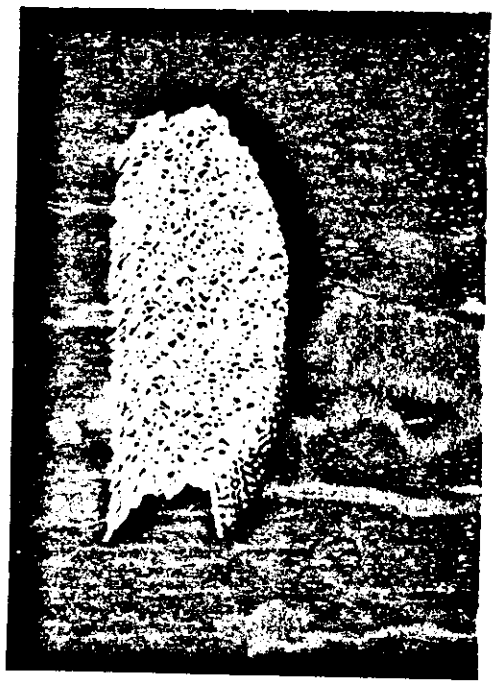

T. 31

In 32

(b)

(c)